catalysts

MDPI

Review

Investigation of Advanced Oxidation Process in the Presence of TiO_2 Semiconductor as Photocatalyst: Property, Principle, Kinetic Analysis, and Photocatalytic Activity

Amir Hossein Navidpour [1], Sedigheh Abbasi [2], Donghao Li [3], Amin Mojiri [4] and John L. Zhou [1,*]

[1] Centre for Green Technology, School of Civil and Environmental Engineering, University of Technology Sydney, 15 Broadway, Sydney, NSW 2007, Australia
[2] Central Research Laboratory, Esfarayen University of Technology, Esfarayen 9661998195, North Khorasan, Iran
[3] Department of Chemistry, Yanbian University, Yanji 133002, China
[4] Department of Civil and Environmental Engineering, Graduate School of Advanced Science and Engineering, Hiroshima University, Higashihiroshima 739-8527, Japan
* Correspondence: junliang.zhou@uts.edu.au

Abstract: Water pollution is considered a serious threat to human life. An advanced oxidation process in the presence of semiconductor photocatalysts is a popular method for the effective decomposition of organic pollutants from wastewater. TiO_2 nanoparticles are widely used as photocatalysts due to their low cost, chemical stability, environmental compatibility and significant efficiency. The aim of this study is to review the photocatalytic processes and their mechanism, reaction kinetics, optical and electrical properties of semiconductors and unique characteristics of titanium as the most widely used photocatalyst; and to compare the photocatalytic activity between different titania phases (anatase, rutile, and brookite) and between colorful and white TiO_2 nanoparticles. Photocatalytic processes are based on the creation of electron–hole pairs. Therefore, increasing stability and separation of charge carriers could improve the photocatalytic activity. The synthesis method has a significant effect on the intensity of photocatalytic activity. The increase in the density of surface hydroxyls as well as the significant mobility of the electron–hole pairs in the anatase phase increases its photocatalytic activity compared to other phases. Electronic and structural changes lead to the synthesis of colored titania with different photocatalytic properties. Among colored titania materials, black TiO_2 showed promising photocatalytic activity due to the formation of surface defects including oxygen vacancies, increasing the interaction with the light irradiation and the lifetime of photogenerated electron–hole pairs. Among non-metal elements, nitrogen doping could be effectively used to drive visible light-activated TiO_2.

Keywords: black TiO_2; colored titania; photocatalytic activity; reaction kinetics; titania phases

check for updates

Citation: Navidpour, A.H.; Abbasi, S.; Li, D.; Mojiri, A.; Zhou, J.L. Investigation of Advanced Oxidation Process in the Presence of TiO_2 Semiconductor as Photocatalyst: Property, Principle, Kinetic Analysis, and Photocatalytic Activity. *Catalysts* **2023**, *13*, 232. https://doi.org/10.3390/catal13020232

Academic Editors: Gassan Hodaifa, Antonio Zuorro, Joaquín R. Dominguez, Juan García Rodríguez, José A. Peres, Zacharias Frontistis and Mha Albqmi

Received: 16 December 2022
Revised: 12 January 2023
Accepted: 15 January 2023
Published: 19 January 2023

1. Introduction

Water scarcity is known as the greatest threat to natural ecosystems and human health, especially in arid areas of the world. Economic development and population growth have led to an increase in water demand and reduction of water availability consequently [1]. It is estimated that there will be one billion people living in the arid area suffering from absolute water scarcity by 2025. Thus, people living in such areas will be forced into a reduction of water consumption in agricultural sectors and transmitting water to other parts, which could reduce their domestic food production. Organic wastes, which originate from different industrial products such as dyes, plastics, pesticides, and detergents, are toxic pollutants that could lead to serious diseases in humans. Although wastewater treatment has been extensively used for the degradation of organic pollutants, persistent organic pollutants (POPs) are resistant to degradation and could remain in the treated water [2].

In addition, there are different indoor air pollutants, which could result in wide-ranging health problems.

Different methods have been used for the degradation of organic pollutants in water, including sonochemical degradation [3,4], advanced oxidation process (AOP) [5–10], adsorption [11,12], micellar-enhanced ultrafiltration (MEUF) [13,14], electrochemical oxidation (EO) [15,16], precipitation [17], coagulation [17,18], biodegradation [19], ion exchange [20,21] and forward/reverse osmosis [22,23]. It is notable that each of these processes has advantages and disadvantages. AOPs are divided into various techniques including photo-Fenton process, heterogeneous photocatalysis, ozonation, Fenton process and H_2O_2 photolysis [24]. In general, AOPs have been proposed for poorly biodegradable organic pollutants [2]. Extremely highly reactive hydroxyl radicals (•OH), which are known as the (secondary) oxidant agents in these processes, are formed by primary oxidants (such as ozone or hydrogen peroxide) and are capable of oxidizing various organic pollutants. The hydroxyl radicals, which are the common aspect of all AOPs, are among the non-selective and powerful oxidants that could react through three mechanisms: the transfer of electrons, the abstraction of hydrogen and the addition of radicals. Thus, they can be potentially used for the degradation of complex chemical structures such as refractory species [25,26]. Although AOPs need input of chemicals and energy [27], they are becoming more efficient processes, e.g., photocatalysis. Around 60% of the expenses of photocatalytic reactors could be allocated to the energy consumption [28]. AOPs have a major advantage, as they are capable of partial or even complete degradation of pollutants. In comparison, coagulation, flocculation and membrane processes concentrate pollutants within one phase or transfer them from one phase to another [29].

Environmental photocatalysis has received remarkable attention since the discovery of the TiO_2 photocatalytic activity in 1972 [30]. The oil crisis was one of the reasons that encouraged research in non-fossil fuels in the early 1970s. Moreover, searching for renewable energy sources is another major driver [31]. After their first observation over water splitting by TiO_2, the photocatalytic reduction of CO_2 by different inorganic photocatalysts was reported by Fujishima et al. in 1979 [32]. SnO_2, TiO_2, and ZnO have been extensively used for photocatalytic decomposition of organic pollutants. Despite its several advantages, the removal efficiency of organic pollutants in the presence of a tin semiconductor is not that promising, limiting its use compared to main semiconductors [33–36], whereas TiO_2 and ZnO semiconductor nanoparticles are widely used for the photocatalytic removal of organic pollutants. In general, TiO_2 and ZnO might act as electron acceptors/donors when irradiated [37]. Because of its transparency, compatibility with the environment, and suitable band gap, ZnO has attracted the attention of many researchers for photocatalytic activities [38,39]. ZnO has three main crystallite structures including wurtzite, rocksalt, and zinc blend. Noteworthy, wurtzite is its most stable polymorph at ambient temperature and pressure [40]. Although ZnO has shown higher photo-absorption ability than TiO_2, it suffers from photocorrosion while exposed to UV irradiation [10]. Overall, TiO_2 (as an ideal semiconductor) has attracted the attention of many researchers due to its unique properties such as significant physicochemical stability, low cost, non-toxicity, electronic and optical properties, as well as abundance, in various fields such as pigments, catalysts, mineral membranes, dielectric materials and removal of pollutants [41,42]. TiO_2 nanoparticles have shown higher photocatalytic activity than bulk TiO_2 (due to larger surface area). The properties of TiO_2 nanoparticles, including morphology, crystal structure, composition of phases, degree of crystallinity, specific surface area, and band gap are influenced by the synthesis method [43–45]. TiO_2 nanoparticles have three major crystal structures including anatase, rutile, and brookite with unique band gap energies of 3.2, 3.0, and 3.1 eV, respectively. Notably, anatase phase with its wider band gap energy than other titania polymorphs has received more attention for photocatalytic activities [44]. The crystal structure of the main phases of titania, i.e., anatase, rutile, and brookite, could be explained by various arrangements of TiO_6 octahedra (Ti^{4+} surrounded by six O^{2-}). Hence, 3-D assembly of TiO_6 octahedra and different degrees of distortion are differences between

these crystal structures. Crustal structures of anatase, rutile, and brookite TiO_2 are exhibited in Figure 1 [46]. Noteworthy, the blue and red balls represent Ti and O atoms, respectively.

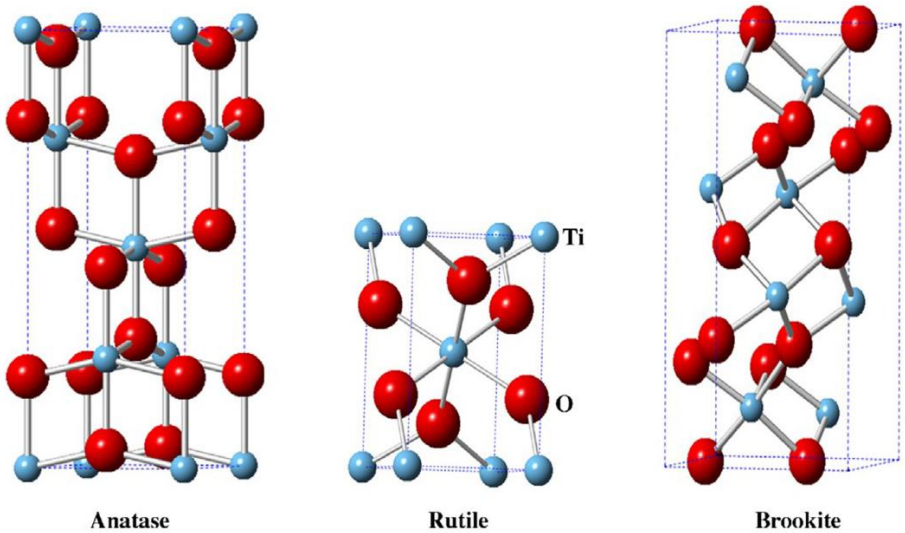

Figure 1. Crystal structures of brookite, rutile, and anatase TiO_2. Reprinted with permission from Ref. [46]. Copyright 2015, Elsevier.

Photocatalysis is a branch of research that uses photons' energy to initiate chemical reactions, which has been inspired by natural photosynthesis [31]. Photocatalytic (PC) and photosynthetic (PS) devices are different technologies that show sensitivity to charge-transfer kinetics, carrier mobility and specific surface area though at varying degrees [47].

From the viewpoint of thermodynamics, chemical reactions are divided into uphill and downhill categories. The schematic of these reactions is illustrated in Figure 2 (the '*' sign could represent the transition state). Uphill reactions that are powered by light could not be considered as photocatalysis [31]. Thermodynamically uphill reactions are nonspontaneous, and the use of a canonical catalyst could not initiate these reactions [31]. Usually, photocatalysis is considered as an appropriate terminology to describe a large number of spontaneous chemical reactions (downhill reactions) that are hindered by high activation energies. Thus, the introduction of light, as a source of energy, could enable these reactions [31,47]. Notably, there is another group of reactions that borrows the photocatalysis term. These reactions that use external potentials, usually, are referred to as photo-electrocatalytic/photo-electrochemical reactions [31]. Unlike photocatalysis, the photo-electrochemical water splitting is a thermodynamically uphill reaction [48–50]. Thus, during the process of photocatalytic water splitting, the energy of photons is converted to chemical energy (by using a photocatalytic material) [50].

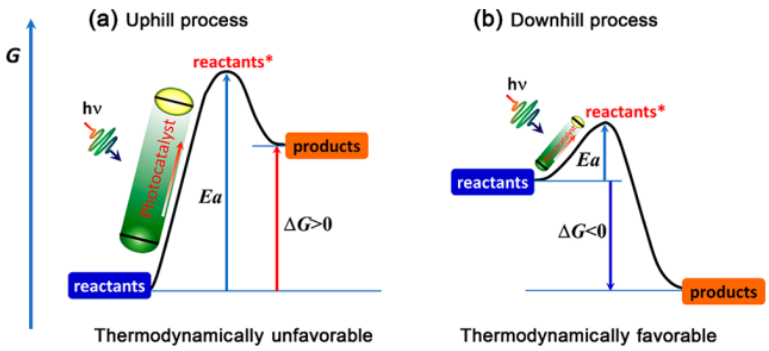

Figure 2. The schematic illustration of (**a**) uphill and (**b**) downhill reactions. Reprinted with permission from Ref. [51]. Copyright 2018, American Chemical Society.

The fundamental principles of photocatalysis and photocatalytic activity of various kinds of semiconducting materials have been widely evaluated by researchers, especially in recent years. Although this process is well-known as an efficient process for water and wastewater treatment, several key points should be further considered to facilitate the use of this process for practical applications. Firstly, the use of promising photocatalytic materials increasing the proficiency of this process is of high importance. Moreover, the expansion of the scope of reactions should receive more attention. For example, TiO_2 has found applications in building materials (for antifogging and self-cleaning properties) and antibacterial materials since the discovery of its super hydrophilicity [52]. Super hydrophilicity is an effect observed for materials whose surfaces display water contact angles (WCAs) below 10° [53]. Super hydrophilicity and photocatalysis are two simultaneous phenomena occurring upon the illumination of TiO_2 [54]. The attempt to degrade emerging pollutants plays an important role in the development and practical applications of this process. However, broad applications of this process would be unlikely without consideration of an appropriate method of photocatalyst immobilization. Another key point is that 3–6% of the solar spectrum is from the ultraviolet radiation [55], while TiO_2, as the most common photocatalytic material, has negligible visible-light adsorption. Since about 43% of the solar spectrum is allocated to visible light [56], attempts are intensifying currently to drive visible-light activated photocatalysts. In recent years, photocatalytic processes in the presence of semiconductors have attracted the attention of many researchers for the removal and decomposition of organic pollutants. Several factors such as photocatalyst type, structure, synthesis method and doping with metallic or non-metallic elements could affect the efficiency of semiconductors. Therefore, the main goal of this study is to review the kinetics of photocatalytic reactions and specifically clarify the photocatalytic properties of TiO_2 with different phases and colors.

2. Photocatalysis

2.1. Principles

Overall, semiconductor photocatalysis relies on four steps as follows [31]:

a. Absorption of photons with equal/larger energy than the bandgap energy of semiconductor under irradiation of light that results in the photogeneration of electron and hole pairs;
b. Charge carrier separation;
c. Transfer of charge carriers to the surface of semiconducting material;
d. Redox reactions initiated by charge carriers.

The photogeneration of electron and hole pairs could be followed by the generation of active species [57,58]. These highly reactive oxygen species (ROSs), including hydroxyl radicals ($^{\bullet}OH$), superoxide radical ions ($^{\bullet}O_2^{-}$), hydrogen peroxide (H_2O_2), hydroperoxy radicals ($^{\bullet}HO_2$) and singlet oxygen ($^1O_2$), are responsible for further reactions [55,59–61]. The oxidation potential of hydroxyl radical ($E^o(^{\bullet}OH/H_2O$ = 2.8 V) is just below that of fluorine [62]. Notably, the photogenerated e^-/h^+ pairs could migrate through various pathways, as they could migrate to the surface of the semiconductor material. The electron acceptors (A) such as O_2 could receive the photogenerated electrons, and the photogenerated holes could result in the oxidation of donor species (D) under these circumstances. The redox potential levels of the adsorbed species and the position of conduction band (CB) and valence band (VB) play an important role in the rate and probability of the charge transfer processes for photogenerated e^-/h^+ pairs. The more is the lifetime of photogenerated e^-/h^+ pairs, the more quantity of ROS should be produced, which leads to the higher efficiency of photodegradation of organic contaminations in air and water. On the other hand, the recombination of photogenerated e^-/h^+ pairs, which could happen either at the surface or in the bulk of the semiconductor, prevents electron transfer processes and could result in the emission of light or release of heat [63,64]. To yield the highest photocatalytic activity, the recombination rate of charge carriers should be restricted. For such a purpose, several techniques such as heterojunction formation [65], metal deposition [66], creation

of oxygen vacancies [67], and non-metal/metal ion doping [68] have been employed. It is noteworthy that surface reactions take place only if the reduction and oxidation potentials are more positive and negative than CB and VB levels, respectively [69].

The mechanism of an ideal heterogeneous photocatalytic process is based on the Equations (1)–(12) [70–72].

$$\text{Semiconductor} + h\upsilon \rightarrow \text{Semiconductor}\ (h^{+}{}_{VB} + e^{-}{}_{CB}) \quad (1)$$

$$h^{+}{}_{VB} + e^{-}{}_{CB} \rightarrow \text{heat} \quad (2)$$

$$OH^{-} + h^{+}{}_{VB} \rightarrow {}^{\bullet}OH \quad (3)$$

$$H_2O + h^{+}{}_{VB} \rightarrow {}^{\bullet}OH + H^{+} \quad (4)$$

$${}^{\bullet}OH + {}^{\bullet}OH \rightarrow H_2O_2 \quad (5)$$

$$e^{-} + H^{+} + O_2 \rightarrow {}^{\bullet}HO_2 \quad (6)$$

$${}^{\bullet}HO_2 + {}^{\bullet}HO_2 \rightarrow O_2 + H_2O_2 \quad (7)$$

$$O_2 + e^{-} \rightarrow \bullet O_2{}^{-} \quad (8)$$

$$\bullet O_2{}^{-} + H^{+} + {}^{\bullet}HO_2 \rightarrow O_2 + H_2O_2 \quad (9)$$

$$H_2O_2 + e^{-} \rightarrow {}^{\bullet}OH + OH^{-} \quad (10)$$

$$H_2O_2 + {}^{\bullet}OH \rightarrow H_2O + {}^{\bullet}HO_2 \quad (11)$$

$${}^{\bullet}OH + \text{organic substances} \rightarrow \text{intermediate} \rightarrow \text{product} \quad (12)$$

The photocatalytic process in water could be carried out as follows [30]:

a. Transfer of the pollutants from the liquid phase to the surface of catalyst;
b. Pollutants adsorption onto the surface of the activated catalyst;
c. Photogeneration of ROSs, including $^{\bullet}OH$, followed by pollutants degradation;
d. Desorption of intermediates from the surface of catalyst;
e. Transferring intermediates into the liquid phase.

Due to the crucial role of surface reactions in the photocatalysis mechanism, the adsorption of reactants on the surface of the semiconducting material is of great importance [31]. For instance, various mechanisms of oxidation have been observed for the degradation of phenol, benzene, and formic acid using TiO_2 [73]. Formic acid could be chemisorbed strongly on titania in water, which leads to direct oxidation by trapping photogenerated holes. In comparison, benzene is physisorbed on titania and has been photo-oxidized by an indirect transfer mechanism. When it comes to phenol, both chemisorption and physisorption processes could take place, and its photooxidation mechanism depends on the solvent used [31]. In addition to the reactants, the relative binding strength of products/intermediates to the surface of photocatalytic material is of high importance. For instance, the photocurrent decrease of WO_3 in $HClO_4$ has been allocated to the bond of photogenerated species on it, which could hinder the water oxidation of active sites [31]. Another key point is the probable interactions between water and the photocatalysts, which should be considered to determine the mechanism of photocatalytic processes.

2.2. Kinetic Analysis

The classical equation of Langmuir–Hinshelwood (L-H) has been widely used for the kinetic analysis of both liquid-phase and gas-phase photocatalysis [55,74–78]. Using this model, the relationship between the oxidation rate and the concentration of reactant is shown in Equation (13) (when the concentrations of oxygen and water remain constant) [77,78]:

$$r = -\frac{dD}{dt} = \frac{r_L K_L^{app}[D]}{1 + K_L^{app}[D]} \quad (13)$$

where r and [D] are the oxidation rate (mg m^{-3} min^{-1}) and the concentration of reactant (mg m^{-3}), respectively [78]. Langmuir–Hinshelwood parameters are K_L^{app} and r_L that are identified as the apparent Langmuir adsorption constant (m^3 min^{-1}) and the apparent L-H rate constant of the reaction, respectively [78,79].

Equation (13) can be transformed as Equation (14) [77]:

$$\frac{1}{r} = \frac{1}{r_L}\left(1 + \frac{1}{K_L^{app}[D]}\right) \tag{14}$$

The time dependence of the concentration of the adsorbed reactant is given in Equation (15) [77]:

$$\frac{d[D_{ad}]}{d_t} = k_a[D]([S_D] - [D_{ad}]) - k_d[D_{ad}] - k_i I[D_{ad}] \tag{15}$$

where $[S_D]$, k_a, k_d, and k_i are the total concentration of the adsorption site for reactant, adsorption rate constant in the dark, desorption rate constant in the dark, and photoinduced desorption rate constant, respectively. There are some concerns for robotic application of L-H model to interpret the kinetic data [73,79]:

a. Adsorption–desorption equilibrium of substrate species is not disturbed under illumination (as a pre-assumption);
b. Ambiguous photon flow intervention (as an experimental parameter);
c. Issues in intervening physical meaning;
d. Chemical nature of the semiconductor surface does not change during photocatalysis (as a pre-assumption);
e. Disregarding the electronic interaction of surface with substrate species;
f. Considering that chemisorption of organic species onto the surface of catalyst is vital for photocatalysis.

The dark Langmuir adsorption constant (K_L) is not the same as K_L^{app}(usually $K_L^{app} \gg K_L$). It has been shown that k_{LH} is a function of absorbed light intensity (I^β) where β equals 1.0 (at low absorbed light intensity) or 0.5 (at high absorbed light intensity) [80]. After reevaluation of the semiconductor photo-assisted reactions, another simple mechanism has been suggested as follows [80]:

$$D(\text{liquid}) \longleftrightarrow D(\text{ads}) \tag{16}$$

$$D(\text{ads}) \overset{k_{LH}}{\longleftrightarrow} \text{products} \tag{17}$$

It is assumed that the reaction of a surface hydroxyl radical and the absorbed reactant takes place in the latter step, Equation (17), which results in the formation of products. Based on the relationship between this step and absorbed light intensity (and the incident light intensity, consequently) correlation between k_{LH} and I^β has been proposed as follows [80]:

$$k_{LH} = \alpha I^\beta \tag{18}$$

In which α is proportionality constant and β equals 1.0 or 0.5 as discussed above. The surface coverage of the reactant (θ_D) is defined as follows by consideration of a pseudo-steady-state hypothesis [80]:

$$\theta_D = \frac{K_{ads}^{app}[D]}{1 + K_{ads}^{app}[D]} \tag{19}$$

where K_{ads}^{app} is given by Equation (20) as follows [80]:

$$K_{ads}^{app} = \frac{1}{K_{diss}^{app}} = \frac{k_1}{k_{-1} + \alpha I^\beta} \tag{20}$$

K_{diss}^{app} is defined as the apparent dissociation constant. Thus, the oxidation rate, r, is given as follows by considering that $-r = k_{LH}\theta_D$ [80]:

$$-r = \frac{k_{LH}[D]}{K_{diss}^{app} + [D]} \tag{21}$$

Boulamanti et al. have proposed the following equation by studying the photocatalytic activity of target gas and by considering the effect of water vapor [81]:

$$r = k\frac{K_{LH}D}{1 + K_{LH}D + K_w D_w} \tag{22}$$

where K_w is a Langmuir adsorption constant proportional to the adhered water molecules to the surface of the catalyst, and D_w is the concentration of water in the gas-phase.

3. Band Gap Estimation and Quantum Size Effect

Inorganic/organic semiconductors display various physical properties, and thus can be used for a variety of purposes [82]. The optical properties of semiconducting nanomaterials are their band gap energy (E_g) as well as absorption coefficient (K), potentially. The band gap energy of semiconductors is a crucial characteristic of their electronic structure, which determines their potential applications [83]. Although it could be affected by the synthesis/processing method, the exact determination of its value is a challenge in materials science and engineering. In direct band gap semiconductors, the recombination of e^-/h^+ pairs could be radiative, if the VB maximum and CB minimum are aligned in the momentum space, which results in photoluminescence [82]. When it comes to the indirect band gap semiconductors, phonons (lattice vibrations) that are involved in the emission and absorption of light allow the semiconductor to convert the light energy into mechanical (photoacoustic) or thermal (photothermal) responses [82]. When a semiconductor is exposed to photons of energy larger than its band gap, the transfer of electrons from the valence band to the conduction band leads to an abrupt increase in the absorbency of the semiconductor to the wavelength, which corresponds to the band gap energy. The relationship between the incidental photon energy and the absorption coefficient is dependent on the type of band gap (direct or indirect). The electronic properties of semiconductors are usually studied by conversion of DR spectra to pseudo-absorption spectra, $F(R_\infty)$, using the Kubelka–Munk function as follows [83,84]:

$$F(R_\infty) = \frac{K}{S} = \frac{(1 - R_\infty)^2}{2R_\infty} \tag{23}$$

$$R_\infty = \frac{R_{sample}}{R_{standard}} \tag{24}$$

where $F(R_\infty)$ is the Kubelka–Munk function and R_∞ is the diffused reflectance of the non-transparent material with infinite thickness. Thus, the supporting material is not contributed (in the case of semiconductors deposited on a substrate). The S and K parameters are the scattering and absorption K-M coefficients, respectively. It is notable that S does not depend on the wavelength for particles larger than 5 μm. Therefore, S could be considered as a constant and $F(R_\infty)$ could be considered as a pseudo-absorption function, consequently [83]. By far, a combination of absorption-based spectroscopic methods, including diffuse reflectance spectroscopy (DRS) on bulk samples or transmission measurements on thin films and coatings and the Tauc method, is the most common procedure of determination of band gap energy [83]. Since absorption-based spectroscopic methods do not confound bulk properties with surface effects, they are preferable for the measurement of bulk properties [83]. The Tauc method was proposed by Tauc et al. as a method for determination of band gap energy by plotting an optical absorption coefficient against energy while evaluating the electronic and optical properties of amorphous germanium.

The strength of optical absorption is dependent on the difference between the energy of photons and the band gap energy as follows [84]:

$$(\alpha h\nu)^{\frac{1}{n}} = A(E - E_g) \tag{25}$$

where ν is the photon/light frequency, α is the linear absorption coefficient, E_g is the band gap energy, h is the Planck's constant, A is a proportionality constant, and n is a constant that depends on the nature of the electronic transition [84]:

For direct allowed transitions: n = 1/2;
For indirect allowed transitions: n = 2;
For direct forbidden transitions: n = 3/2;
For indirect forbidden transitions: n = 3.

The 'E' term is the incident photon energy and is calculated as follows:

$$E(eV) = h\nu = \frac{hC}{\lambda(nm)} = \frac{1236}{\lambda(nm)} \tag{26}$$

It is notable that the majority of basic absorption processes are allowed transitions (n = 2 or n = 1/2 for indirect and direct transitions, respectively) [84]. Finally, the graph of $(\alpha h\nu)^{\frac{1}{n}}$ vs. hν is plotted, and the band gap energy is easily extrapolated by the interception of the linear region to the X-axis. Usually, different values of n (usually 1, and 1/2) are used to identify the correct type of transition. As an example, the Tauc plot of TiO_2 is shown in Figure 3 [85]. Noteworthy, the straight blue line has been plotted to estimate E_g.

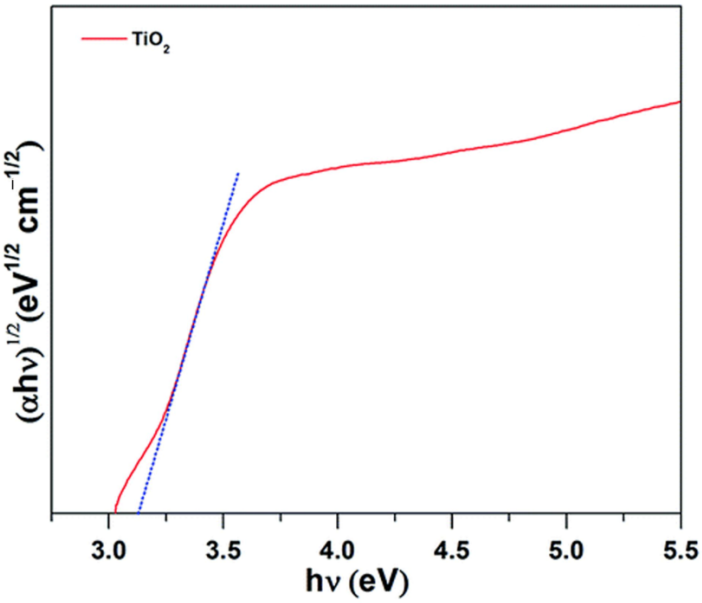

Figure 3. The Tauc plot of TiO_2. Reprinted with permission from Ref. [85]. Copyright 2015, Royal Society of Chemistry.

It is notable that the size of particles could change the band gap energy of semiconductors [55,86]. The planetary model of the Bohr hydrogen atom is generally used for description of the movement of the bonded electron–hole pair originated by photoexcitation. The exciton Bohr radius, a_B, is used for calculation of the region of delocalization of the electron hole pair as follows [86]:

$$a_B = \frac{\hbar^2 \varepsilon}{e^2}\left[\frac{1}{m_e^* m_O} + \frac{1}{m_h^* m_O}\right] \tag{27}$$

where ε is the dielectric constant of the semiconductor, e is the charge of an electron, $\hbar$ is the reduced Planck's constant, m_e^* is the effective mass of electron, m_h^* is the effective mass of hole, and m_O is the rest mass of an electron. The steric limitation of photoexcited charges is observed in the bulk of a semiconductor whose nanocrystals are smaller than the region of delocalization of exciton. This could change some characteristic features of semiconductors. However, the degree of changes depends on the ratio of nanoparticle radius, R, and the value of a_B. In this case, two different modes could be considered [86]:

$a_B \leq$ R: There is a weak restriction in this region so that a similar electronic structure is observed for both the bulk crystal and the nanoparticle.

$a_B >$ R: There is a strong quantum confinement in the region so that a radical rearrangement is observed for the electronic structure of semiconductor nanoparticle. For example, energy of the exciton excitation increases. Moreover, discrete electronic levels are provided by gradual change in the energy bands of the semiconductor.

This phenomenon, in which the top of VB and the bottom of CB shift in positive and negative directions, respectively, is called a quantum-size effect and could result in the expansion of band gap energy. The Bohr radius of rutile and anatase TiO_2 is around 0.3 and 2.5 nm, respectively. Thus, interpreting the results by using quantum-size effect needs deep evaluations, in cases such as TiO_2, since synthesis of such a small size might be difficult [55]. It is noteworthy that the band gap energy of semiconducting nanomaterials could be highly dependent on their morphology. For instance, titania particles with nanoburrs or lateral organization could have lower band gap energies [87]. Based on the band gap energy, semiconductors are divided into two major categories: wide band gap semiconductors and narrow band gap semiconductors. Band gap energies of some major semiconductors are illustrated in Figure 4 [88]. Among different photocatalysts, TiO_2 is used as the most common semiconductor for photocatalytic applications and is discussed in the following part.

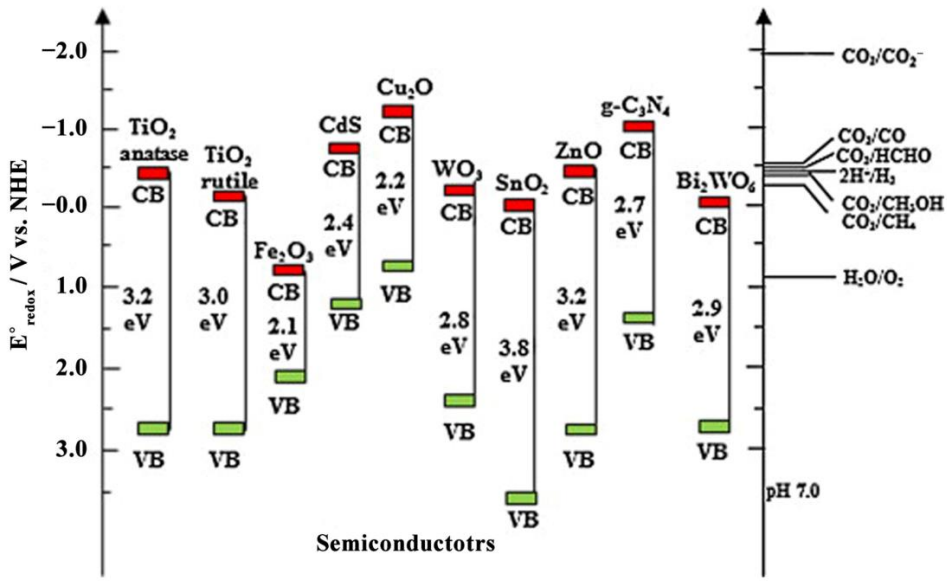

Figure 4. Band gap of major semiconductors (with respect to the redox potential of various chemical species measured at pH 7). Reprinted with permission from Ref. [88]. Copyright 2015, Elsevier.

4. TiO_2

4.1. General Properties and Applications

TiO_2 has found several applications in toothpaste, sunscreens, plastics, printing ink, condensers, paper, electronic components, leather, cosmetics, ceramics, food, and pigmentation since its commercial production [89–91]. High refractive indices of anatase and rutile phases, which lead to high reflectivity from surfaces, takes account for its several applications where white coloration is desired [42,92]. Since the discovery of the photocatalytic

water splitting on a titanium oxide electrode under UV illumination by Fujishima and Honda, serious efforts have been allocated to the study of its efficiency in photocatalysis, photovoltaics, sensors, and photoelectrochemical applications, which can be generally divided into two discrete categories of environmental and energy [93,94]. TiO_2 is non-toxic and earth abundant, and has high photostability [94,95]. It is the most common semiconducting material used for photocatalytic applications and has been employed as a benchmark photocatalyst in many research works (especially commercial Degussa P-25 powder, which consists of both anatase and rutile phases) [96–98]. Although there are various semiconducting materials, an overwhelming majority of researchers (around 60%) have focused on different TiO_2 phases in photocatalytic works during the 2000s [99]. The position of the top valence band of TiO_2 is ca. 3 V vs. NHE (at pH 0). Therefore, the potential of its positive holes is remarkably more positive than oxidation potential of ordinary organic compounds. The valence bands of the majority of metal oxides are composed of the same orbitals (O2p). Thus, most of them possess the same potential of the top valence band and the same oxidation ability is expected for all of them [55]. In addition, the surface chemistry of water and oxygen is fundamental to important processes such as the oxygen reduction reaction (ORR) and photocatalytic water oxidation. These reactions are mediated by photoexcited electrons and holes, respectively. Water oxidation is a hole-mediated process as follows [100]:

$$2H_2O + 4h^+ \rightarrow 4H^+ + O_2 \tag{28}$$

The ORR is a process mediated by photoexcited electrons that is followed by reactions with coadsorbed water as follows [100]:

$$O_2 + e^- \rightarrow (O_2)^- \tag{29}$$

$$OOH^- + e^- \rightarrow OH^- + (O_{ad})^- \tag{30}$$

$$(O_{ad})^- + e^- + H_2O \rightarrow 2OH^- \tag{31}$$

$$H_2O + OOH^- \rightarrow OH^- + H_2O_2 \tag{32}$$

$$(O_2)^- + e^- + H_2O \rightarrow OH^- + OOH^- \tag{33}$$

$$H_2O_2 + 2e^- \rightarrow 2OH^- \tag{34}$$

Although both the ORR and water oxidation involve the same intermediate species (H_2O_2, OH^-, or OOH^-), the identification of the reaction intermediates is not simple (since they are usually short-lived) [100]. To illustrate this point, characteristic times for different photo-reactions in the heterogeneous photocatalysis on TiO_2 are shown in Table 1 [101].

Therefore, one of the probable reasons for high photocatalytic activity of TiO_2 could be its high reduction potential that is responsible for the injection of photogenerated electrons into the molecular O_2 on its surface [55]. Notably, equal numbers of positive holes and electrons must be consumed for completion of photocatalytic reactions. Thus, positive holes cannot be used for oxidation reactions, despite of their high potentials, unless the photogenerated electrons are consumed simultaneously. Most other metal oxides have high oxidation ability; however, their low reduction ability may result in their lower photocatalytic activity compared with TiO_2 [55].

Table 1. Characteristic times for heterogeneous photocatalysis on TiO_2: where e_{cb}^- is the conduction band electron, h_{vb}^+ is the valence band hole, e_{tr}^- is the trapped conduction band electron, >TiOH shows the primary hydrated surface functionality of titania, $>Ti^{IV}OH\bullet+$ is the surface-bound hydroxyl radical, $>Ti^{III}OH$ is the surface-trapped conduction band electron, Red is the reductant, and OX is the oxidant [101].

Type of Primary Reaction	Primary Reaction	Characteristic Time (s)
Generation of charge carriers	$TiO_2 + h\upsilon \rightarrow e_{cb}^- + h_{vb}^+$	fs
Charge carrier trapping	$H_{vb}^+ + > Ti^{IV}OH \rightarrow > \{Ti^{IV}OH\}^+$	10 ns
• Deep trap (irreversible)	$e_{cb}^- + > Ti^{IV} \rightarrow >Ti^{III}$	10 ns
• Shallow trap (dynamic equilibrium)	$e_{cb}^- + > Ti^{IV}OH \leftrightarrow \{>Ti^{III}OH\}$	100 ps
Charge carrier recombination	$h_{vb}^+ + \{> Ti^{III}OH\} \rightarrow >Ti^{IV}OH$	10 ns
	$e_{cb}^- + > \{Ti^{IV}OH^\bullet\}^+ \rightarrow >Ti^{IV}OH$	100 ns
Interfacial charge transfer	$\{>Ti^{IV}OH^\bullet\}^+ + Red \rightarrow > Ti^{IV}OH + Red^{\bullet+}$	100 ns
	$e_{tr}^- + OX \rightarrow Ti^{IV}OH + OX^{\bullet-}$	ms

4.2. Optical and Electrical Properties of TiO_2

In general, rutile TiO_2 is more anisotropic than anatase TiO_2 in the range from infrared to visible spectra. On the other hand, an important anisotropy is observed for anatase phase in the band gap region [102]. Since titania is known as an n-type semiconductor, donor-type defects (e.g., titanium interstitials and oxygen vacancies) are responsible for its conductivity [103]. The excessive electrons in the solid, introduced by oxygen vacancies, could enhance the electrical conductivity [102]. However, oxidized titania may show p-type properties as a result of concurrent presence of acceptor-type defects including titanium vacancies. $Ti_{1-x}O_2$ or TiO_{2+x} could be applied, instead of TiO_2, where titanium vacancies could make a remarkable contribution to the defect disorder (under prolonged oxidation conditions) [103]. Doping is an efficient method that could be used to form both n-type and p-type titania. For example, manganese-doped TiO_2 has shown p-type electrical conduction [104,105]. In addition to manganese, iron, nickel, chromium and cobalt could act as electron acceptors. Thus, Fe-doped [106,107], Ni-doped [108], Cr-doped [109–111] and Co-doped [112,113] TiO_2 could show p-type electrical conduction. The ratio between the concentration of metal dopants and that of oxygen vacancies could be crucial to the reduction or augment of the electrical conductivity. In addition to the concentration of oxygen vacancies, their contribution should also be taken into account for evaluation of the electrical conductivity [102]. On the other hand, niobium and tantalum could act as electron donors. Therefore, W-doped [114], Ta-doped [115], and Nb-doped [116,117] TiO_2 could show n-type electrical conduction.

Various non-metal elements including N, P, S, B, and I have been extensively employed to drive visible-light-activated TiO_2. Among those, N-doping has received remarkable attention as a method efficiently used for driving visible-light activated TiO_2 [118–122]. It has been shown that nitrogen-doping could remarkably reduce the formation energy of oxygen vacancies as confirmed by DFT calculations. Thus, N-doped TiO_2 can take advantage of the presence of oxygen vacancies (especially on its surface) [123]. By far, various methods have been used for the synthesis of N-doped TiO_2 including sputtering, sol-gel, chemical vapor deposition, decomposition of nitrogen-containing metal-organic precursors, spray pyrolysis, pulsed laser deposition, combustion reaction, high-energy milling, and implantation. Schematic illustrations of models for doping of different nitrogen species including substitutional N-doping, interstitial N-doping, substitutional NO-doping, substitutional NO_2-doping, and interstitial NO-doping are shown in Figure 5.

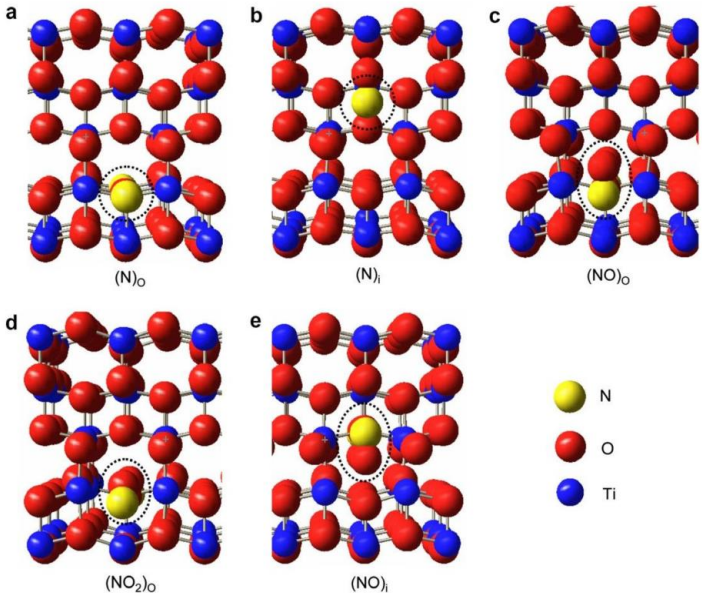

Figure 5. Schematic models for (**a**) substitutional N-doping, (**b**) interstitial N-doping, (**c**) substitutional NO-doping, (**d**) substitutional NO_2-doping, and (**e**) interstitial NO-doping. Reprinted with permission from Ref. [124]. Copyright 2007, Elsevier.

Thus, nitrogen doping into a TiO_2 lattice structure could be either interstitial or substitutional. Peng et al. synthesized both interstitial and substitutional N-doped TiO_2 for photocatalytic degradation of methyl orange and phenol. They suggested that although both interstitial and substitutional nitrogen doping could drive visible-light activated TiO_2, interstitial N-doped TiO_2 could show a higher photocatalytic activity than that of substitutional N-doped TiO_2 [125]. Zeng et al. compared the photocatalytic activity of visible-light activated interstitial and substitutional N-doped TiO_2 toward degradation of benzene under the same conditions (similar grain size, crystallinity, and specific surface area of the as-prepared samples) [126]. Unlike Peng et al., they concluded that substitutional N-doped TiO_2 could show higher photocatalytic activity than that of interstitial N-doped TiO_2. Lower recombination rate of the photogenerated e^-/h^+ pairs and higher proportion of surface hydroxyl groups have accounted for the higher photocatalytic activity of substitutional N-doped TiO_2. The higher photocatalytic activity of interstitial N-doped TiO_2 than that of substitutional N-doped TiO_2, as reported by Peng et al. [125], could originate from different methods used by Peng et al. for the synthesis of interstitial and substitutional N-doped TiO_2 [126]. It should be noted that the photocatalytic activity of semiconductors could be highly influenced by their grain/particle size [127–129], specific surface area [130–132], and crystallinity/polymorph [133–135]. Of note, nitrogen doping could be achieved through simultaneous interstitial and substitutional doping as confirmed by XPS analysis [136]. In substitutional doping, either oxygen atoms or titanium atoms can be substituted by nitrogen atoms. Therefore, $TiO_{2-x}N_x$ (titanium oxynitride) and $Ti_{1-y}O_{2-x}N_{x+y}$ are the results of the substitution of oxygen atoms and substitution of both oxygen and titanium atoms by nitrogen atoms, respectively. As suggested by Peng et al., $Ti_{1-y}O_{2-x}N_{x+y}$ could be formed at high concentrations of nitrogen (as high as 21 mol%) [137]. Valentin et al. suggested that nitrogen doping is likely accompanied by the formation of oxygen vacancies. Besides, they proposed that the abundance of nitrogen-doping species is dependent on the preparation conditions including the annealing temperature and the oxygen concentration (in the atmosphere) [138]. As for the substitutional N-doped TiO_2 (N-Ti-O and Ti-O-N), localized N 2p states (slightly above the VB of pure TiO_2) could be responsible for the visible-light response [139]. Migration of photo-excited electrons from VB to the N 2p states could reduce the band gap energy of TiO_2 [136]. Notably, NO bond with π-character that generates new localized states (slightly above the VB of pure TiO_2) accounts for the

visible-light response of interstitial N-doped TiO_2 [139]. Valentin et al. suggested that the highest localized states for the interstitial and substitutional nitrogen species are 0.73 and 0.14 eV above the top of the valence band, respectively [140]. Not only could interstitial and substitutional nitrogen doping increase the visible-light harvest, but it could also intensify the absorption of UV-light, which originates from the appearance of defect energy levels in the band gap [126].

It has been shown that the photocatalytic efficiency of titania could be strongly correlated to its (micro) structure and semiconducting properties [103,141]. Additionally, the electrical properties of titania nanostructures depend on the crystallographic directions [102]. It is why the evaluation of the electrical properties of TiO_2 is of high importance for photocatalytic applications, as shown in Table 2.

Table 2. Comparison of the crystal structural, optical and electrical properties for TiO_2 nanostructures. Adapted with permission from Ref. [102]. Copyright 2018, Royal Society of Chemistry. This article is licensed under a Creative Commons Attribution-NonCommercial 3.0 Unported Licence (https://creativecommons.org/licenses/by-nc/3.0/) (Accessed on 1 December 2022).

Properties	TiO_2 Nanostructures		
	Rutile	**Anatase**	**Brookite**
Crystal Structure	Tetragonal	Tetragonal	Orthorhombic
Lattice constant (A)	a = 4.5936 c =2.9587	a = 3.784 c = 9.515	a = 9.184 b = 5.447 c = 5.154
Molecule (cell)	2	2	4
Volume/molecule (A°3)	31.21	34.061	32.172
Density (g cm^{-3})	4.13	3.79	3.99
Ti–O bond length (A°)	1.949 (4) 1.980 (2)	1.937 (4) 1.965 (2)	1.87–2.04
O–Ti–O bond angle	81.2° 90°	77.7° 92.6°	77 − 105°
Band gap at 10 K	3.051 eV	3.46 eV	
Static dielectric constant (ε_0, in MHz range)	173	48	
High frequency dielectric constant, ε_∞ ($\lambda = 600$ nm)	8.35	6.25	

When defects are electrically charged, defect disorder could largely affect the electrical properties. There are several reports on the investigation of the electrical properties of rutile TiO_2 at high temperatures and in nanocrystalline form [142–146]. Although evaluation of the electrical properties of anatase TiO_2 is of interest, several experimental problems, owing to its grain growth and partial phase transformation into rutile at elevated temperatures, has prevented its widespread studies [141]. The electrical properties of oxide semiconductors including titania are generally temperature dependent. This dependency is generally considered by the activation energy of electrical conductivity [103,147]. It is notable that the oxygen partial pressure could play a crucial role in the activation energy of electrical conductivity of single-crystal (SC) and polycrystalline (PC) TiO_2 [147]. The electrical conductivity of metals and n-type semiconductors including TiO_2 is the reciprocal of their resistivity and could be expressed as follows [147,148]:

$$\sigma = \frac{1}{\rho} = en\mu_n \tag{35}$$

in which σ is the electrical conductivity, ρ is the resistivity, n is the concentration of electrons, μ_n is the mobility of electrons, and e is the elementary charge [147]. Based on the four probe method, sample dimensions are required to determine the resistivity and/or electrical conductivity as follows [148]:

$$\rho = R\frac{L}{A} \tag{36}$$

where R, A, and L are resistance, surface area of the cross section, and distance between voltage electrodes, respectively [148]. The mobility is defined as follows [149]:

$$\mu_n = \frac{\nu}{\varepsilon} \tag{37}$$

The mobility is usually determined by scattering with photons (in an intrinsic semiconductor). The mobility's of electrons (μ_n) for some semiconductors such as Si, Ge, GaAs, GaN, InSb, InAs, InP, and ZnO are 1300, 4500, 8800, 300, 77,000, 33,000, 4600, and 230 cm^2/Vs, respectively, and the mobilities of holes (μ_p) for the same semiconductors are 500, 3500, 400, 180, 750, 460, 150, and 8 cm^2/Vs, respectively. Usually, semiconductors possess a much higher mobility than that of metals including Cu (i.e., 35 cm^2/Vs) [149]. In the case of TiO_2, the slope of log σ versus log p (O_2), which is dependent on the oxygen activity, is −1/6 and −1/4 in highly reduced conditions ($p(O_2) < 10^{-5}$ Pa) and in oxidized conditions ($p(O_2) > 10$ Pa), respectively (at elevated temperatures).

4.3. Promising Phases of TiO_2 for Photocatalytic Applications

Titanium dioxide, which is an n-type semiconductor owing to the presence of oxygen vacancies, crystalizes naturally in three major different phases including anatase (tetragonal), brookite (orthorhombic) and rutile (tetragonal). Among all TiO_2 polymorphs, anatase and rutile phases are generally used in photocatalytic applications [150]. However, brookite TiO_2 could also find applications in photocatalysis [151–154]. It has shown a higher photocatalytic activity than that of rutile TiO_2 in some cases. For instance, hydrothermally synthesized brookite TiO_2 has exhibited superior photocatalytic activity than that of hydrothermally synthesized rutile TiO_2 in degradation of some hazardous pharmaceuticals (ibuprofen, diatrizoic acid, and cinnamic acid) and phenol as model organic pollutant. The higher efficiency of the brookite phase (in this case study) has been devoted to the existence of highly active species, superoxide radicals and valence band holes, in the photocatalytic treatment [155]. In another study, titania nanoparticles (including pure anatase, anatase-rich, pure brookite, and brookite-rich phases) have been synthesized by Kandiel et al. for photocatalytic purposes.

Interestingly, higher photocatalytic activity was observed by using as-prepared brookite titania nanoparticles compared with as-prepared anatase TiO_2 nanoparticles. The surface area of the latter has been three times higher than that of the former. The higher photocatalytic efficiency of brookite titania nanoparticles for methanol photooxidation has been devoted to their higher crystallinity and/or to the cathodic shift of the CB of brookite TiO_2 compared with that of anatase TiO_2, which could facilitate the transfer of interfacial electrons to the molecular oxygen [156]. Although anatase and rutile TiO_2 are the most common titania polymorphs used for photocatalytic applications, it has been shown that brookite TiO_2 could exhibit markedly high photocatalytic activity, even higher than the anatase phase, in some cases (e.g., for degradation of ibuprofen, cinnamic acid, and phenol, and photooxidation of methanol) [152,156]. However, brookite titania has not received great attention due to some limitations such as its difficult synthesis procedure to generate high purities [157]. Of note, rutile TiO_2 is thermodynamically stable at ambient conditions [156] while anatase is a meta-stable phase. The band gap energy of rutile phase is lower than that of the anatase phase with the band gap energy of ~3.2 eV [158]. The phase transition between titania polymorphs depends on several factors. For instance, particle size, surface area, heating rate, particle shape (aspect ratio), volume of sample, atmosphere, measurement technique, soaking time, nature of sample container, and impurities are among various factors that affect the phase transformation of undoped anatase to rutile TiO_2 [92]. The transition of anatase to rutile is a reconstructive process in which the Ti-O bonds are ruptured. Afterwards, a structural rearrangement and formation of new Ti-O bonds occur which result in the formation of rutile phase. It is worth mentioning that the phase transformation of anatase to rutile is a nucleation and growth process [92]. However, it has been shown that this transition is limited by nucleation stage and not by growth. It

should be considered that when it comes to the phase transition of nanocrystalline anatase, both surface and interface nucleation processes could be observed though at varying rates. The experiments have confirmed that interface nucleation is more rapid than surface nucleation [159]. Usually, rutile phase nucleates at (112) twin interfaces, in pure anatase, because of similar structure of these sites to rutile phase [92]. Upon heating, both meta-stable brookite and anatase phases could transform to rutile phase, irreversibly, though at different temperatures [92,158,160]. Notably, this transformation could take place at different temperatures and various attempts have been made to promote/inhibit it [92]. When it comes to the pure synthetic TiO_2, it could occur between 600–700 °C [160]. According to the report of Wu et al. [161], the effect of temperature on the phase stability and crystallite size of TiO_2 is shown in Figure 6.

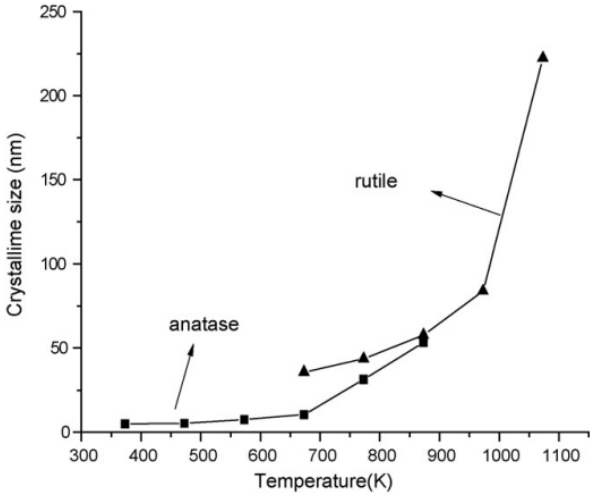

Figure 6. Effect of thermal treatment temperature on crystallite size of TiO_2. Reprinted with permission from Ref. [161]. Copyright 2007, Elsevier.

As evident, an increase in the temperature could result in an increase in the crystallite size of both anatase and rutile TiO_2 (though at different degrees). Although the transformation of anatase to rutile has been widely studied, the transformation of brookite to anatase or vice versa is a bit controversial. The transformation of anatase to rutile could be carried out either directly or indirectly. However, some reports suggest that the brookite phase transforms to the anatase phase at first. Then, anatase TiO_2 transforms to rutile TiO_2. On the other hand, there are some reports suggesting that the anatase phase transforms to the brookite and/or rutile phases prior to the transformation of brookite to rutile [156].

Accordingly, the anatase and brookite phases are not stable at large crystallite sizes. In another words, the most thermodynamically stable phases of TiO_2 are rutile, brookite, and anatase, respectively (by increasing the crystallite sizes). Thermodynamic studies have also confirmed the higher stability of the rutile phase than the anatase phase at all positive temperatures and pressures. The results are shown in Figure 7.

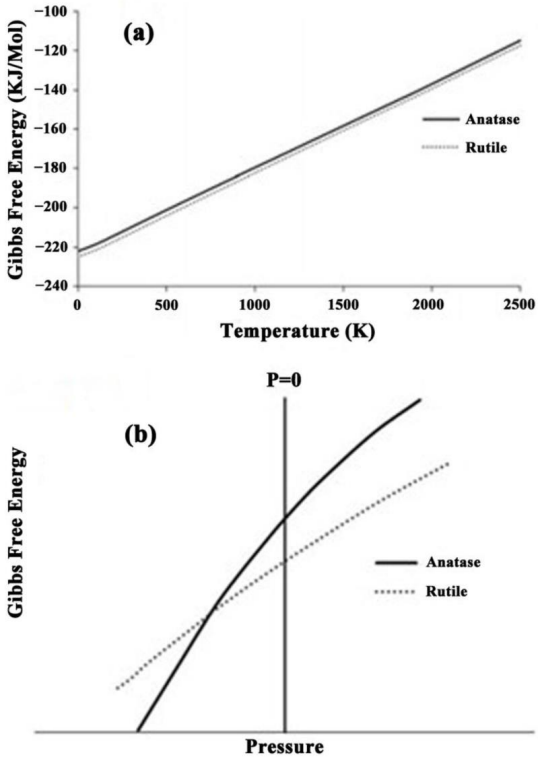

Figure 7. Plots of Gibbs free energy of anatase and rutile versus (**a**) temperature and (**b**) pressure (at room temperature). Reprinted with permission from Ref. [92]. Copyright 2011, Springer.

Bulk and/or surface doping of TiO_2 could affect the stability of anatase and rutile phases and change the temperature of the transition of anatase to rutile, which has been explained by a ceased crystal growth as the result of the formation of Ti-O-M bonds. For instance, doping with metal cations including Nd [162], La [163], Ni [164], Si, W, Cr [165], Al, Nb, Ga, and Ta [166] could retard the grain/particle growth of anatase and rutile phases and delays the transition of anatase to rutile. The addition of molybdenum and tungsten could completely eliminate the anatase phase at temperatures between 680 and 830 °C, respectively [102]. Doping with V, Ag, Mn [165], Zn, Fe and Cu [166] could generally promote this transformation. However, there are some dual behaviors which should be considered. For example, Wang et al. have reported the acceleration of anatase to rutile phase transition for Nb-doped TiO_2. It is while a depression effect has been observed on the grains growth of anatase for Nb-doped TiO_2 [165]. Using cationic/anionic dopants [167] and non-metal dopants, including carbon [168], nitrogen [169], fluorine [170,171] and chlorine [171] could affect the phase transformation of titania. Unlike interstitial atoms that could increase the strain energy that must be overcome and the bonds that must be broken, the creation of oxygen vacancies, originated from the incorporation of ions with relatively small ionic radius and lower valence than that of Ti^{4+}, could facilitate the phase transformation by reduction of the strain energy needed for the rearrangement of the Ti-O octahedra. The rate of the transition of anatase to rutile strongly depends on the incorporated dopants [172].

4.4. Photocatalytic Activity of Anatase Titania Compared with Its Other Polymorphs

It is generally believed that among the anatase, rutile, and brookite phases, the anatase phase is responsible for photocatalytic reactions. There are some statements that a pure rutile phase could not have any photocatalytic activity at all. However, some believe that it could possess photocatalytic activity, which depends on the nature of the organic reactant, preparation method of the photocatalyst and the nature of the precursor materials [150]. Considering pure phases, the anatase phase could provide higher photocatalytic activity

than rutile TiO_2 [46,98]. The higher photocatalytic activity of anatase phase than other polymorphs could be attributed to its higher mobility of charge pairs and density of surface hydroxyl [46]. Notably, discrepancy with the recombination kinetics of e^-/h^+ pairs might also play an important role in the superior photocatalytic efficiency of anatase phase as photoluminescence (PL) studies for anatase TiO_2 have clarified its lower recombination rate of charge carriers than that of rutile phase under similar condition [173]. Brookite and rutile TiO_2 are direct band gap semiconductors, while anatase TiO_2 belongs to the category of indirect band gap semiconductors [174]. For indirect band gap semiconductors, the electronic transition from the VB to the CB is electrical dipole forbidden. Under these circumstances, the transition results in the change of both momentum and energy of the photogenerated e^-/h^+ pairs (transition is phonon assisted). On the other hand, the valence band to the conduction band electronic transition is electrical dipole allowed for direct band gap semiconductors. Due to the momentum change, the electronic absorption/emission of indirect band gap semiconductors is weaker than that of direct band gap semiconductors [175]. Thus, direct band gap semiconductors, such as rutile TiO_2, have more efficient absorption of solar energy than indirect ones (such as anatase TiO_2) [174,175]. However, a longer diffusion length as well as lifetime of photogenerated e^-/h^+ pairs could result in better photocatalytic performance of anatase TiO_2 than its rutile phase [174]. In addition, it has been reported that the anatase phase is more active than the rutile phase in absorption of hydroxyl groups and water [150] that could play an important role in photocatalysis. A schematic of recombination processes of photoexcited e^-/h^+ pairs within anatase TiO_2 (indirect gap) and rutile TiO_2 (direct gap) is shown in Figure 8 [174].

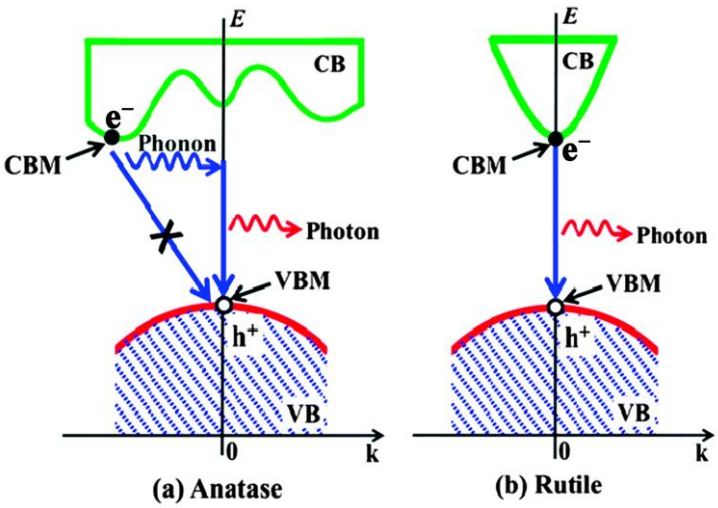

Figure 8. Schematic of recombination processes of photoexcited e^-/h^+ pairs within (**a**) anatase TiO_2 and (**b**) rutile TiO_2. Reprinted with permission from Ref. [174]. Copyright 2014, Royal Society of Chemistry.

In addition to the band gap nature, the diffusion of free charge carriers is of remarkable importance. To achieve appropriate photocatalytic efficiency, the photoexcited e^-/h^+ pairs should migrate to the active sites where they are used prior to the recombination process. In this context, the diffusion of photogenerated e^-/h^+ pairs is strongly linked to their mobility, which is in turn related to their effective mass. The ratio of the effective mass of electrons to effective mass of holes is used to predict the stability of photogenerated e^-/h^+ pairs with respect to their recombination. In this case, a larger effective mass difference could enhance the photocatalytic activity as the result of the reduction of the e^-/h^+ pair recombination [176]. In general, the transfer rate of photoexcited e^-/h^+ pairs that affects the quantum efficiency of photocatalysts could be assessed by the effective mass of electrons and holes [174].

As evident, there is an inverse relationship between the transfer rate of photoexcited e^-/h^+ pairs and the effective mass of charge carriers. To sum up, the smaller the effective mass of charge carriers, the faster the transfer rate of charge carriers. Anatase TiO_2 has a lighter average effective mass of photoexcited e^-/h^+ pairs than that of both the brookite and rutile phases, which leads to the faster migration of e^-/h^+ pairs from bulk titania to its surface. This results in its lower recombination rate of photoexcited e^-/h^+ pairs [174]. It should be noted that there is not yet consensus on the reasons for higher photocatalytic activity of the anatase phase than that of the rutile and brookite phases [177]. It is worth mentioning that there are various factors, including method of synthesis, concentration of defects, purity of phases, surface crystallographic orientation, particle size, dopants, specific surface area, and its crystal structure (type of polymorph), that could remarkably affect the photocatalytic activity of TiO_2 [46,98].

4.5. Colorful TiO_2 versus White TiO_2

Recently, colored titania materials such as green, red, yellow, blue, brown and grey of various shades have been developed. The colorful titania could be synthesized by electronic and structural changes such as the incorporation of Ti-OH and Ti-H species, formation of oxygen vacancies, formation of disordered surface layers, reduction of Ti^{4+} to Ti^{3+}, narrowed band gap energy, and the modified electron density [178]. These could result in the synthesis of green, red, black, and grey materials [179]. Black TiO_2, synthesized by Chen et al. using high pressure hydrogenation, has shown a largely narrowed band gap energy (for massive visible light absorption) and an enhanced photocatalytic activity. Since then, it has received remarkable attention in visible light utilization. Notably, the optical absorption of black titania could be extended to the IR region (approximately 1150 nm) [178]. The importance of black titania has resulted in its various applications in photocatalytic water splitting, photoelectron chemical water splitting, photocatalysis, fuel cells, Li-ion batteries, Na-ion batteries, Al-ion batteries, surface enhanced Raman active scattering substrate, supercapacitors, cancer photothermal therapy, solar desalination, microwave absorption, field emission, and dye sensitized solar cells (DSSC) [180,181]. Various methods, such as low pressure hydrogen treatment, high pressure hydrogen treatment, argon treatment, hydrogen–nitrogen treatment, hydrogen–argon treatment, hydrogen–plasma treatment, chemical oxidation, chemical reduction, electrochemical reduction, pulsed laser ablation, and hydroxylation, have been used to synthesize black titania nanomaterials [180].

Black titania, synthesized by hydrogenation, was firstly used for photocatalytic degradation of methylene blue and phenol [182]. Since then, photodegradation of methylene blue, as a model of organic pollutants, has been studied by many researchers using this polymorph of titania [182–184]. It is worth mentioning that black TiO_2 has shown a higher photocatalytic activity than that of white TiO_2 in several cases [184,185].

It has been stated that the formation of some surface defects, including oxygen vacancies and/or Ti^{3+} oxidation states, and disordered layers in the surface of highly crystalline TiO_2, could increase the interaction to the light irradiation and the lifetime of photogenerated electron/hole pairs [184]. However, Ti^{3+} ions have not been observed in some samples of black TiO_2. Thus, oxygen vacancies could be known as the main factor responsible for black coloration of titania [186]. The superior photocatalytic activity and/or photo electrochemical properties of black TiO_2 than pristine TiO_2 or P25 have also been reported by other researchers some of which are given in Table 3.

Table 3. Superior photocatalytic and photoelectrochemical properties of black TiO_2 than white TiO_2 in some case studies.

Synthesis Method	Light Source	Improvement of Photocatalytic Activity	Improvement of Photoelectrochemical Properties	References
Melted aluminum reduction of pristine anodized and air-annealed TiO_2 nanotube arrays	The simulated sunlight (intensity of 100 mW cm^{-2})	-	Approximately 5 times higher than pristine TiO_2 nanotube arrays	[187]
Electrospinning process	A 150 W xenon lamp	-	Approximately a 10-fold increase compared with pristine TiO_2 nanofibers	[188]
In situ plasma hydration of TiO_2 thin films	A 150 W xenon lamp (intensity of 100 mW cm^{-2})	-	Approximately 2.5 times higher than pristine TiO_2 thin films	[189]
Electrochemical reductive doping	• UV source: A UV lamp (intensity of 5.8 mW cm^{-2}) • Visible-light source: A xenon lamp (intensity of 100 mW cm^{-2})	-	Approximately 2.2 times higher than pristine anodic TiO_2 nanotubes (under both UV and simulated solar irradiation)	[190]
Using Ti_2O_3 as precursor for preparing Ti^{3+} self-doped TiO_2 nanowires	A 20 W UV lamp	Approximately 7.5 times higher than pure TiO_2 (P25) in photodegradation of methyl orange	-	[191]
hydrogen plasma assisted chemical vapour deposition	A 50 W simulated solar light source	Complete photodegradation of rhodamine B after approximately 30 min against partial photodegradation of rhodamine B even after 50 min for pure TiO_2	-	[192]
Annealing the TiO_2 nanobelts in hydrogen atmosphere	• UV source: A 350 W mercury lamp • Visible-light source: A 300 W xenon arc lamp	• UV illumination: An approximate increase of 24% compared with pristine TiO_2 nanobelts in decomposing methyl orange • Visible light irradiation: An approximate increase of 17% compared with pristine TiO_2 nanobelts in decomposing methyl orange	-	[193]
Annealing the TiO_2 nanobelts in hydrogen atmosphere	A 300 W xenon arc lamp	-	Approximately 9.2 times higher than pristine TiO_2 nanobelts	[193]

Oxygen vacancies are among the most important/common point defects originated by removal of some neutral oxygen atoms from the lattice structure of metal oxides including TiO_2 [194]. However, the major defect could become tetravalent titanium interstitials under extremely reduced conditions that are experimentally difficult to achieve [103]. In general, the driving force for the creation of vacancies is minimizing the Helmholtz free energy to establish thermodynamic equilibrium at a specific temperature. Cations and anions are two different types of vacancy defects in ionic crystals that lead to the formation of localized energy levels over the VB maximum and below the CB minimum, respectively [194]. The formation of oxygen vacancies could result in the development of Ti^{3+} species (by filling the empty states of titanium ions using excesses electrons originated from removal of oxygen atoms) [195,196] and the formation of shallow donor states under the CB of titania originating from Ti 3d orbits [195]. Owing to the higher active surface area of nanomaterials than that of bulk materials, a higher number of oxygen vacancies could be stimulated in

the surface and subsurface regions of nanostructured titania than bulk titania. In addition, titania nanocrystals have less formation energy of oxygen vacancies than their bulk counterpart, which is why the creation of oxygen vacancies and evaluation of their effect in TiO_2 nanomaterials have received greater attention. Oxygen vacancies possess the minimum formation energy among the defects that could act as donors. Therefore, they have received great attention in defining chemical and physical properties of materials (including superconductivity, ferromagnetism, photocatalysis, resistive switching, phase transitions, redox activity, piezoelectric response, and photoelectrochemical performance) [194]. Hydrogen thermal treatment, high energy particle bombardment, doping of metal or non-metal ions, thermal treatment under oxygen depleted conditions, and some special reaction conditions are common methods used for development of TiO_2 with oxygen vacancies [195]. Thermal treatment under oxygen deficient conditions could be considered as an efficient method for creation of oxygen vacancies in TiO_2-based nanomaterials [194]. This process is performed at elevated temperatures, usually > 400 °C, in vacuum or pure Ar, He, and N_2 gas atmosphere [195].

The decrease of oxygen pressure results in an increase of the concentration of oxygen vacancies; hence, thermal treatment of titania under oxygen deficient conditions could facilitate the creation of oxygen vacancies. Therefore, the exposure of titania to air leads to the gradual removal of oxygen vacancies [195]. Doping with accept-type foreign ions, including Fe and Zn, could stabilize the as-formed oxygen vacancies [95,195]. Oxygen vacancies on anatase phase and rutile phase have been widely studied since they could be engineered/generated at mild conditions [196]. The calculation of the formation energy of oxygen vacancies has confirmed that creation of oxygen vacancies at the top surface of anatase (101) and (001) planes is more probable than other planes (because of their lower formation energies of vacancies). In comparison, rutile (110) planes have lower vacancy formation energy than that of other rutile crystalline planes [194]. Oxygen vacancies are capable of introducing localized states into the band gap structure (instead of the change of positions of valence band and conduction band). The driving force for development of these localized states is the Madelung potential of highly ionic crystal [195]. Transition of electrons from the oxygen vacancies to the valence band and/or from the valence band to the oxygen vacancies leads to infrared- and visible-light absorption [185,186]. Additionally, they act as potential shallow traps for significant improvement of the efficiency of electron–hole separation [184,186]. The energy level position of oxygen vacancies, which form a donor level under the conduction band of TiO_2, is from 0.75 to 1.18 eV [185,186,195]. It is worth mentioning that experimental and theoretical studies show that the excess electrons, originated from the formation of the oxygen vacancies, could affect the reactivity and surface absorption of important adsorbents including H_2O and O_2 on titania. These are some reasons why development of TiO_2 with the desired amount of oxygen vacancies is of great importance [195].

In addition to black TiO_2, other colored titania materials (including red, green, blue, yellow, and various shades of grey titania) have also found applications in photocatalysis and photoelectrochemical water splitting due to their specific features. For instance, Liu et al. have synthesized anatase titania microspheres with an interstitial $B^{\sigma+}$ ($\sigma \leq 3$) gradient shell, red TiO_2, that are capable of absorbing the full visible light spectrum. UV-visible absorption of the white TiO_2 and these red TiO_2 microspheres are compared in Figure 9 (black and red graphs, respectively) [197]. Noteworthy, the colorful region represents the visible light spectrum ranged from 400 to 700 nm.

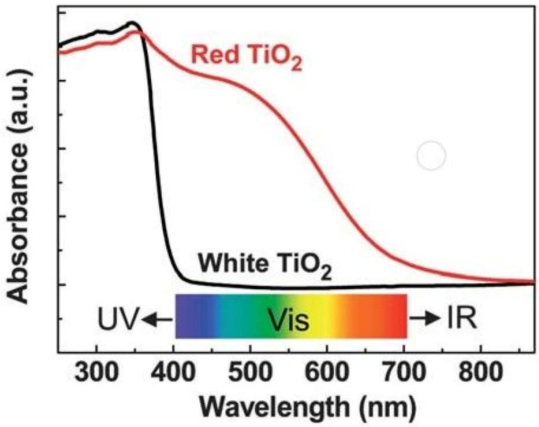

Figure 9. Comparison of UV-visible absorption of the white TiO_2 and red TiO_2 microspheres. Reprinted with permission from Ref. [197]. Copyright 2012, Royal Society of Chemistry.

As evident, red titania microspheres possess much higher photo absorption ability than white titania in the visible light range. These microspheres have provided a gradient of absorption band gap energy from 1.94 eV (on their surface) to 3.22 eV (in their core) [179,197]. It has also been reported that red anatase TiO_2-based materials could show an unusual visible-light absorption that is representative of new types of visible light absorption bands of titania [198]. Thus, red titania-based photoanodes could be used for photoelectrochemical water splitting under visible-light irradiation [197,198]. Some other colorful titania-based photoanodes, including blue TiO_2, could be inactive in photoelectrochemical water oxidation under visible-light irradiation [198].

5. Conclusions and Perspectives

The application of TiO_2 semiconductor nanoparticles for the photocatalytic decomposition of pollutants in wastewater has been considered in this study. Considering that TiO_2 has three different structures (anatase, rutile and brookite), their stability and photocatalytic efficiency were compared. It should be noted that the band gap energy of these three crystal structures is different. In addition to the effect of band gap energy, the photocatalytic activity is influenced by the degree of stability and separation of the produced electron–hole pairs which could be dependent on the mobility as well as the mass ratio of the electron to the hole. Among the existing phases, the rutile phase has relatively high stability at different temperatures and pressures. The photocatalytic activity of titanium depends on its structure and morphology. Investigations show that the photocatalytic activity of anatase phase is higher than that of rutile and brookite. Although some studies indicate that the rutile phase does not have any photocatalytic activity, studies show that the rutile phase can be used for photocatalytic processes, which depends on the structure of the pollutant, the preparation method, and the precursor material of the photocatalyst. In general, the photocatalytic activity depends on the stability of the produced electron–hole pairs. Increasing the stability and separation of the created charges leads to a decrease in their recombination and an increase in the photocatalytic efficiency. Studies show that the photocatalytic activity of titania is also dependent on its color. Electronic and structural changes such as the combination of Ti-OH and Ti-H species, the formation of oxygen vacancies, the formation of irregular surface layers, and the reduction of Ti^{4+} to Ti^{3+} are among the effective factors in the formation of colored titania. Black titania has a largely narrowed band gap energy which leads to the enhancement of photocatalytic activity.

Due to their stability and adverse effects on human health and environment, the application of colorful TiO_2 in the degradation of persistent organic pollutants is worth studying. It should be noted that photocatalysis cannot find practical applications without immobilization of catalysts, due to the several issues encountered by using nanoparticles including agglomeration and difficulty of recovery. Moreover, immobilization could fa-

cilitate the application of photoelectrocatalysis with its superior efficiency than custom photocatalysis. Hence, the application of surface engineering methods in the deposition of colorful TiO_2 films for photocatalytic degradation of persistent organic pollutants is of high importance in future studies.

Author Contributions: A.H.N.: conceptualization, writing—original draft, writing—review and editing; S.A.: writing—original draft, D.L.: writing—review and editing; A.M.: writing—review and editing; J.L.Z.: supervision, writing—review and editing. All authors have read and agreed to the published version of the manuscript.

Funding: This research received no external funding.

Data Availability Statement: Not applicable.

Acknowledgments: This work is supported by the University of Technology Sydney. The author Sedigheh Abbasi is grateful for the support by the Esfarayen University of Technology.

Conflicts of Interest: All authors undertake that they have no conflict of interest.

References

1. Liu, J.; Yang, H.; Gosling, S.N.; Kummu, M.; Flörke, M.; Pfister, S.; Hanasaki, N.; Wada, Y.; Zhang, X.; Zheng, C.; et al. Water scarcity assessments in the past, present, and future. *Earth's Future* **2017**, *5*, 545–559. [CrossRef] [PubMed]
2. Ong, C.B.; Ng, L.Y.; Mohammad, A.W. A review of ZnO nanoparticles as solar photocatalysts: Synthesis, mechanisms and applications. *Renew. Sustain. Energy Rev.* **2018**, *81*, 536–551. [CrossRef]
3. Wei, Z.; Spinney, R.; Ke, R.; Yang, Z.; Xiao, R. Effect of pH on the sonochemical degradation of organic pollutants. *Environ. Chem. Lett.* **2016**, *14*, 163–182. [CrossRef]
4. Debabrata, P.; Sivakumar, M. Sonochemical degradation of endocrine-disrupting organochlorine pesticide Dicofol: Investigations on the transformation pathways of dechlorination and the influencing operating parameters. *Chemosphere* **2018**, *204*, 101–108. [CrossRef] [PubMed]
5. Deng, Y.; Zhao, R. Advanced oxidation processes (AOPs) in wastewater treatment. *Curr. Pollut. Rep.* **2015**, *1*, 167–176. [CrossRef]
6. Navidpour, A.H.; Hosseinzadeh, A.; Huang, Z.; Li, D.; Zhou, J.L. Application of machine learning algorithms in predicting the photocatalytic degradation of perfluorooctanoic acid. *Catal. Rev. Sci. Eng.* **2022**, 1–26. [CrossRef]
7. Navidpour, A.H.; Fakhrzad, M. Photocatalytic activity of Zn_2SnO_4 coating deposited by air plasma spraying. *Appl. Surf. Sci. Adv.* **2021**, *6*, 100153. [CrossRef]
8. Navidpour, A.H.; Fakhrzad, M. Photocatalytic and magnetic properties of $ZnFe_2O_4$ nanoparticles synthesised by mechanical alloying. *Int. J. Environ. Anal. Chem.* **2022**, *102*, 690–706. [CrossRef]
9. Navidpour, A.H.; Salehi, M.; Amirnasr, M.; Salimijazi, H.R.; Azarpour Siahkali, M.; Kalantari, Y.; Mohammadnezhad, M. Photocatalytic iron oxide coatings produced by thermal spraying process. *J. Therm. Spray Technol.* **2015**, *24*, 1487–1497. [CrossRef]
10. Navidpour, A.H.; Salehi, M.; Salimijazi, H.R.; Kalantari, Y.; Azarpour Siahkali, M. Photocatalytic activity of flame-sprayed coating of zinc ferrite powder. *J. Therm. Spray Technol.* **2017**, *26*, 2030–2039. [CrossRef]
11. Dai, Y.; Zhang, N.; Xing, C.; Cui, Q.; Sun, Q. The adsorption, regeneration and engineering applications of biochar for removal organic pollutants: A review. *Chemosphere* **2019**, *223*, 12–27. [CrossRef] [PubMed]
12. Wang, J.; Zhuang, S. Removal of various pollutants from water and wastewater by modified chitosan adsorbents. *Crit. Rev. Environ. Sci. Technol.* **2017**, *47*, 2331–2386. [CrossRef]
13. Schwarze, M. Micellar-enhanced ultrafiltration (MEUF)—State of the art. *Environ. Sci. Water Res. Technol.* **2017**, *3*, 598–624. [CrossRef]
14. Hussain, K.I.; Usman, M.; Siddiq, M.; Rasool, N.; Nazar, M.F.; Ahmad, I.; Holder, A.A.; Altaf, A.A. Application of micellar enhanced ultrafiltration for the removal of sunset yellow dye from aqueous media. *J. Dispers. Sci. Technol.* **2017**, *38*, 139–144. [CrossRef]
15. Mojiri, A.; Ohashi, A.; Ozaki, N.; Shoiful, A.; Kindaichi, T. Pollutant removal from synthetic aqueous solutions with a combined electrochemical oxidation and adsorption method. *Int. J. Environ. Res. Public Health* **2018**, *15*, 1443. [CrossRef]
16. Parsa, J.B.; Shojaat, R. Removal of organic dye pollutants from wastewater by electrochemical oxidation. *Phys. Chem. Liq.* **2007**, *45*, 479–485. [CrossRef]
17. Kim, Y.; Osako, M.; Lee, D. Removal of hydrophobic organic pollutants by coagulation-precipitation process with dissolved humic matter. *Waste Manag. Res.* **2002**, *20*, 341–349. [CrossRef]
18. Ren, X.; Xu, X.; Xiao, Y.; Chen, W.; Song, K. Effective removal by coagulation of contaminants in concentrated leachate from municipal solid waste incineration power plants. *Sci. Total Environ.* **2019**, *685*, 392–400. [CrossRef]
19. Belhaj, D.; Baccar, R.; Jaabiri, I.; Bouzid, J.; Kallel, M.; Ayadi, H.; Zhou, J.L. Fate of selected estrogenic hormones in an urban sewage treatment plant in Tunisia (North Africa). *Sci. Total Environ.* **2015**, *505*, 154–160. [CrossRef]

20. Jorgensen, T.C.; Weatherley, L.R. Ammonia removal from wastewater by ion exchange in the presence of organic contaminants. *Water Res.* **2003**, *37*, 1723–1728. [CrossRef]
21. Feng, Y.; Yang, S.; Xia, L.; Wang, Z.; Suo, N.; Chen, H.; Long, Y.; Zhou, B.; Yu, Y. In-situ ion exchange electrocatalysis biological coupling (i-IEEBC) for simultaneously enhanced degradation of organic pollutants and heavy metals in electroplating wastewater. *J. Hazard. Mater.* **2019**, *364*, 562–570. [CrossRef] [PubMed]
22. Cui, Y.; Liu, X.-Y.; Chung, T.-S.; Weber, M.; Staudt, C.; Maletzko, C. Removal of organic micro-pollutants (phenol, aniline and nitrobenzene) via forward osmosis (FO) process: Evaluation of FO as an alternative method to reverse osmosis (RO). *Water Res.* **2016**, *91*, 104–114. [CrossRef]
23. Zhang, A.; Gu, Z.; Chen, W.; Li, Q.; Jiang, G. Removal of refractory organic pollutants in reverse-osmosis concentrated leachate by Microwave–Fenton process. *Environ. Sci. Pollut. Res.* **2018**, *25*, 28907–28916. [CrossRef] [PubMed]
24. Rasalingam, S.; Peng, R.; Koodali, R.T. Removal of hazardous pollutants from wastewaters: Applications of TiO_2-SiO_2 mixed oxide materials. *J. Nanomater.* **2014**, *2014*, 617405. [CrossRef]
25. Dewil, R.; Mantzavinos, D.; Poulios, I.; Rodrigo, M.A. New perspectives for advanced oxidation processes. *J. Environ. Manag.* **2017**, *195*, 93–99. [CrossRef]
26. Kurniawan, T.A.; Lo, W.-h. Removal of refractory compounds from stabilized landfill leachate using an integrated H_2O_2 oxidation and granular activated carbon (GAC) adsorption treatment. *Water Res.* **2009**, *43*, 4079–4091. [CrossRef] [PubMed]
27. Oller, I.; Malato, S.; Sánchez-Pérez, J.A. Combination of advanced oxidation processes and biological treatments for wastewater decontamination—A review. *Sci. Total Environ.* **2011**, *409*, 4141–4166. [CrossRef] [PubMed]
28. Bandara, J.; Pulgarin, C.; Peringer, P.; Kiwi, J. Chemical (photo-activated) coupled biological homogeneous degradation of p-nitro-o-toluene-sulfonic acid in a flow reactor. *J. Photochem. Photobiol. A Chem.* **1997**, *111*, 253–263. [CrossRef]
29. Paździor, K.; Bilińska, L.; Ledakowicz, S. A review of the existing and emerging technologies in the combination of AOPs and biological processes in industrial textile wastewater treatment. *Chem. Eng. J.* **2019**, *376*, 120597. [CrossRef]
30. Ahmed, S.N.; Haider, W. Heterogeneous photocatalysis and its potential applications in water and wastewater treatment: A review. *Nanotechnology* **2018**, *29*, 342001. [CrossRef]
31. Zhu, S.; Wang, D. Photocatalysis: Basic principles, diverse forms of implementations and emerging scientific opportunities. *Adv. Energy Mater.* **2017**, *7*, 1700841. [CrossRef]
32. Inoue, T.; Fujishima, A.; Konishi, S.; Honda, K. Photoelectrocatalytic reduction of carbon dioxide in aqueous suspensions of semiconductor powders. *Nature* **1979**, *277*, 637–638. [CrossRef]
33. Ghaderi, A.; Abbasi, S.; Farahbod, F. Synthesis, characterization and photocatalytic performance of modified ZnO nanoparticles with SnO_2 nanoparticles. *Mater. Res. Express* **2018**, *5*, 065908–065918. [CrossRef]
34. Abbasi, S.; Hasanpour, M. The effect of pH on the photocatalytic degradation of methyl orange using decorated ZnO nanoparticles with SnO_2 nanoparticles. *J. Mater. Sci. Mater. Electron.* **2017**, *28*, 1307–1314. [CrossRef]
35. Abbasi, S.; Ekrami-Kakhki, M.-S.; Tahari, M. Modeling and predicting the photodecomposition of methylene blue via ZnO–SnO_2 hybrids using design of experiments (DOE). *J. Mater. Sci. Mater. Electron.* **2017**, *28*, 15306–15312. [CrossRef]
36. Xu, B.; Liu, S.; Zhou, J.L.; Zheng, C.; Jin, W.; Chen, B.; Zhang, T.; Qiu, W. PFAS and their substitutes in groundwater: Occurrence, transformation and remediation. *J. Hazard. Mater.* **2021**, *412*, 125159. [CrossRef]
37. Nur, H.; Misnon, I.I.; Wei, L.K. Stannic oxide-titanium dioxide coupled semiconductor photocatalyst loaded with polyaniline for enhanced photocatalytic oxidation of 1-Octene. *Int. J. Photoenergy* **2007**, *2007*, 098548. [CrossRef]
38. Roozban, N.; Abbasi, S.; Ghazizadeh, M. The experimental and statistical investigation of the photo degradation of methyl orange using modified MWCNTs with different amount of ZnO nanoparticles. *J. Mater. Sci. Mater. Electron.* **2017**, *28*, 7343–7352. [CrossRef]
39. Abbasi, S.; Hasanpour, M.; Ekrami-Kakhki, M.-S. Removal efficiency optimization of organic pollutant (methylene blue) with modified multi-walled carbon nanotubes using design of experiments (DOE). *J. Mater. Sci. Mater. Electron.* **2017**, *28*, 9900–9910. [CrossRef]
40. Navidpour, A.H.; Hosseinzadeh, A.; Zhou, J.L.; Huang, Z. Progress in the application of surface engineering methods in immobilizing TiO_2 and ZnO coatings for environmental photocatalysis. *Catal. Rev. Sci. Eng.* **2021**, 1–52. [CrossRef]
41. Abbasi, S. Investigation of the enhancement and optimization of the photocatalytic activity of modified TiO_2 nanoparticles with SnO_2 nanoparticles using statistical method. *Mater. Res. Express* **2018**, *5*, 066302. [CrossRef]
42. Abbasi, S. The degradation rate study of methyl orange using MWCNTs@TiO_2 as photocatalyst, application of statistical analysis based on Fisher's F distribution. *J. Clust. Sci.* **2022**, *33*, 593–602. [CrossRef]
43. Mazinani, B.; Masrom, A.K.; Beitollahi, A.; Luque, R. Photocatalytic activity, surface area and phase modification of mesoporous SiO_2–TiO_2 prepared by a one-step hydrothermal procedure. *Ceram. Int.* **2014**, *40*, 11525–11532. [CrossRef]
44. Réti, B.; Major, Z.; Szarka, D.; Boldizsár, T.; Horváth, E.; Magrez, A.; Forró, L.; Dombi, A.; Hernádi, K. Influence of TiO_2 phase composition on the photocatalytic activity of TiO_2/MWCNT composites prepared by combined sol–gel/hydrothermal method. *J. Mol. Catal. A Chem.* **2016**, *414*, 140–147. [CrossRef]
45. Siah, W.R.; Lintang, H.O.; Shamsuddin, M.; Yuliati, L. High photocatalytic activity of mixed anatase-rutile phases on commercial TiO_2 nanoparticles. *IOP Conf. Ser. Mater. Sci. Eng.* **2016**, *107*, 012005. [CrossRef]
46. Etacheri, V.; Valentin, C.D.; Schneider, J.; Bahnemann, D.; C.Pilla, S. Visible-light activation of TiO_2 photocatalysts: Advances in theory and experiments. *J. Photochem. Photobiol. C Photochem. Rev.* **2015**, *25*, 1–29. [CrossRef]

47. Osterloh, F.E. Photocatalysis versus photosynthesis: A sensitivity analysis of devices for solar energy conversion and chemical transformations. *ACS Energy Lett.* **2017**, *2*, 445–453. [CrossRef]
48. Zhou, X.; Dong, H.; Ren, A.-M. Exploring the mechanism of water-splitting reaction in NiOx/β-Ga2O3 photocatalysts by first-principles calculations. *Phys. Chem. Chem. Phys.* **2016**, *18*, 11111–11119. [CrossRef]
49. Yu, F.; Zhou, H.; Huang, Y.; Sun, J.; Qin, F.; Bao, J.; Goddard, W.A.; Chen, S.; Ren, Z. High-performance bifunctional porous non-noble metal phosphide catalyst for overall water splitting. *Nat. Commun.* **2018**, *9*, 2551. [CrossRef]
50. Leung, D.Y.C.; Fu, X.; Wang, C.; Ni, M.; Leung, M.K.H.; Wang, X.; Fu, X. Hydrogen production over titania-based photocatalysts. *ChemSusChem* **2010**, *3*, 681–694. [CrossRef]
51. Yang, X.; Wang, D. Photocatalysis: From fundamental principles to materials and applications. *ACS Appl. Energy Mater.* **2018**, *1*, 6657–6693. [CrossRef]
52. Wang, R.; Hashimoto, K.; Fujishima, A.; Chikuni, M.; Kojima, E.; Kitamura, A.; Shimohigoshi, M.; Watanabe, T. Light-induced amphiphilic surfaces. *Nature* **1997**, *388*, 431–432. [CrossRef]
53. Otitoju, T.A.; Ahmad, A.L.; Ooi, B.S. Superhydrophilic (superwetting) surfaces: A review on fabrication and application. *J. Ind. Eng. Chem.* **2017**, *47*, 19–40. [CrossRef]
54. Kazemi, M.; Mohammadizadeh, M.R. Simultaneous improvement of photocatalytic and superhydrophilicity properties of nano TiO_2 thin films. *Chem. Eng. Res. Des.* **2012**, *90*, 1473–1479. [CrossRef]
55. Ohtani, B. Preparing articles on photocatalysis—Beyond the illusions, misconceptions, and speculation. *Chem. Lett.* **2008**, *37*, 216–229. [CrossRef]
56. Kong, D.; Zheng, Y.; Kobielusz, M.; Wang, Y.; Bai, Z.; Macyk, W.; Wang, X.; Tang, J. Recent advances in visible light-driven water oxidation and reduction in suspension systems. *Mater. Today* **2018**, *21*, 897–924. [CrossRef]
57. Abbasi, S.; Dastan, D.; Ţălu, Ş.; Tahir, M.B.; Elias, M.; Tao, L.; Li, Z. Evaluation of the dependence of methyl orange organic pollutant removal rate on the amount of titanium dioxide nanoparticles in MWCNTs-TiO_2 photocatalyst using statistical methods and Duncan's multiple range test. *Int. J. Environ. Anal. Chem.* **2022**, 1–15. [CrossRef]
58. Abbasi, S. Improvement of photocatalytic decomposition of methyl orange by modified MWCNTs, prediction of degradation rate using statistical models. *J. Mater. Sci. Mater. Electron.* **2021**, *32*, 14137–14148. [CrossRef]
59. Gui, M.M.; Chai, S.-P.; Xu, B.-Q.; Mohamed, A.R. Enhanced visible light responsive MWCNT/TiO_2 core–shell nanocomposites as the potential photocatalyst for reduction of CO_2 into methane. *Sol. Energy Mater. Sol. Cells* **2014**, *122*, 183–189. [CrossRef]
60. Wang, D.; Li, Y.; Li Puma, G.; Wang, C.; Wang, P.; Zhang, W.; Wang, Q. Mechanism and experimental study on the photocatalytic performance of Ag/AgCl @ chiral TiO_2 nanofibers photocatalyst: The impact of wastewater components. *J. Hazard. Mater.* **2015**, *285*, 277–284. [CrossRef]
61. Gentili, P.L.; Penconi, M.; Costantino, F.; Sassi, P.; Ortica, F.; Rossi, F.; Elisei, F. Structural and photophysical characterization of some $La_{2x}Ga_{2y}In_{2z}O_3$ solid solutions, to be used as photocatalysts for H_2 production from water/ethanol solutions. *Sol. Energy Mater. Sol. Cells* **2010**, *94*, 2265–2274. [CrossRef]
62. Babu, D.S.; Srivastava, V.; Nidheesh, P.V.; Kumar, M.S. Detoxification of water and wastewater by advanced oxidation processes. *Sci. Total Environ.* **2019**, *696*, 133961. [CrossRef]
63. Wang, W.; Huang, G.; Yu, J.C.; Wong, P.K. Advances in photocatalytic disinfection of bacteria: Development of photocatalysts and mechanisms. *J. Environ. Sci.* **2015**, *34*, 232–247. [CrossRef] [PubMed]
64. Linsebigler, A.L.; Lu, G.; Yates, J.T. Photocatalysis on TiO_2 surfaces: Principles, mechanisms, and selected results. *Chem. Rev.* **1995**, *95*, 735–758. [CrossRef]
65. Peng, L.; Xie, T.; Lu, Y.; Fan, H.; Wang, D. Synthesis, photoelectric properties and photocatalytic activity of the Fe_2O_3/TiO_2 heterogeneous photocatalysts. *Phys. Chem. Chem. Phys.* **2010**, *12*, 8033–8041. [CrossRef]
66. Guo, H.; Kemell, M.; Heikkilä, M.; Leskelä, M. Noble metal-modified TiO_2 thin film photocatalyst on porous steel fiber support. *Appl. Catal. B Environ.* **2010**, *95*, 358–364. [CrossRef]
67. Liu, L.; Gao, F.; Zhao, H.; Li, Y. Tailoring Cu valence and oxygen vacancy in Cu/TiO_2 catalysts for enhanced CO_2 photoreduction efficiency. *Appl. Catal. B Environ.* **2013**, *134–135*, 349–358. [CrossRef]
68. Akpan, U.G.; Hameed, B.H. The advancements in sol–gel method of doped-TiO_2 photocatalysts. *Appl. Catal. A Gen.* **2010**, *375*, 1–11. [CrossRef]
69. Wen, J.; Xie, J.; Chen, X.; Li, X. A review on g-C3N4-based photocatalysts. *Appl. Surf. Sci.* **2017**, *391*, 72–123. [CrossRef]
70. Diesen, V.; Jonsson, M. Formation of H_2O_2 in TiO_2 photocatalysis of oxygenated and deoxygenated aqueous systems: A probe for photocatalytically produced hydroxyl radicals. *J. Phys. Chem. C* **2014**, *118*, 10083–10087. [CrossRef]
71. Zhang, J.; Nosaka, Y. Mechanism of the OH radical generation in photocatalysis with TiO_2 of different crystalline types. *J. Phys. Chem. C* **2014**, *118*, 10824–10832. [CrossRef]
72. Navidpour, A.H.; Kalantari, Y.; Salehi, M.; Salimijazi, H.R.; Amirnasr, M.; Rismanchian, M.; Azarpour Siahkali, M. Plasma-sprayed photocatalytic zinc oxide coatings. *J. Therm. Spray Technol.* **2017**, *26*, 717–727. [CrossRef]
73. Montoya, J.F.; Peral, J.; Salvador, P. Comprehensive kinetic and mechanistic analysis of TiO_2 photocatalytic reactions according to the direct–indirect model: (I) Theoretical approach. *J. Phys. Chem. C* **2014**, *118*, 14266–14275. [CrossRef]
74. Monllor-Satoca, D.; Gómez, R.; González-Hidalgo, M.; Salvador, P. The "Direct–Indirect" model: An alternative kinetic approach in heterogeneous photocatalysis based on the degree of interaction of dissolved pollutant species with the semiconductor surface. *Catal. Today* **2007**, *129*, 247–255. [CrossRef]

75. Ollis, D.F. Kinetics of liquid phase photocatalyzed reactions: An illuminating approach. *J. Phys. Chem. B* **2005**, *109*, 2439–2444. [CrossRef] [PubMed]
76. Ollis, D.F. Kinetics of photocatalyzed reactions: Five lessons learned. *Front. Chem.* **2018**, *6*, 1–7. [CrossRef]
77. Nosaka, Y.; Nosaka, A.Y. Langmuir–Hinshelwood and light-intensity dependence analyses of photocatalytic oxidation rates by two-dimensional-ladder kinetic simulation. *J. Phys. Chem. C* **2018**, *122*, 28748–28756. [CrossRef]
78. Tseng, T.-K.; Lin, Y.; Chen, Y.; Chu, H. A review of photocatalysts prepared by sol-gel method for VOCs removal. *Int. J. Mol. Sci.* **2010**, *11*, 2336–2361. [CrossRef]
79. Emeline, A.V.; Ryabchuk, V.K.; Serpone, N. Dogmas and misconceptions in heterogeneous photocatalysis. Some enlightened reflections. *J. Phys. Chem. B* **2005**, *109*, 18515–18521. [CrossRef]
80. Mills, A.; Wang, J.; Ollis, D.F. Kinetics of liquid phase semiconductor photoassisted reactions: Supporting observations for a pseudo-steady-state model. *J. Phys. Chem. B* **2006**, *110*, 14386–14390. [CrossRef]
81. Boulamanti, A.K.; Philippopoulos, C.J. Photocatalytic degradation of C5–C7 alkanes in the gas–phase. *Atmos. Environ.* **2009**, *43*, 3168–3174. [CrossRef]
82. Jiang, Y.; Tian, B. Inorganic semiconductor biointerfaces. *Nat. Rev. Mater.* **2018**, *3*, 473–490. [CrossRef] [PubMed]
83. Dolgonos, A.; Mason, T.O.; Poeppelmeier, K.R. Direct optical band gap measurement in polycrystalline semiconductors: A critical look at the Tauc method. *J. Solid State Chem.* **2016**, *240*, 43–48. [CrossRef]
84. Viezbicke, B.D.; Patel, S.; Davis, B.E.; Birnie Iii, D.P. Evaluation of the Tauc method for optical absorption edge determination: ZnO thin films as a model system. *Phys. Status Solidi B* **2015**, *252*, 1700–1710. [CrossRef]
85. Bansal, A.; Kumar, A.; Kumar, P.; Bojja, S.; Chatterjee, A.K.; Ray, S.S.; Jain, S.L. Visible light-induced surface initiated atom transfer radical polymerization of methyl methacrylate on titania/reduced graphene oxide nanocomposite. *RSC Adv.* **2015**, *5*, 21189–21196. [CrossRef]
86. Stroyuk, O.; Kryukov, A.; Kuchmii, S.; Pokhodenko, V. Quantum size effects in semiconductor photocatalysis. *Theor. Exp. Chem.* **2005**, *41*, 207–228. [CrossRef]
87. Zhang, H.; Zhang, H.; Zhu, P.; Huang, F. Morphological effect in photocatalytic degradation of direct blue over mesoporous TiO_2 catalysts. *ChemistrySelect* **2017**, *2*, 3282–3288. [CrossRef]
88. Ola, O.; Maroto-Valer, M.M. Review of material design and reactor engineering on TiO_2 photocatalysis for CO_2 reduction. *J. Photochem. Photobiol. C Photochem. Rev.* **2015**, *24*, 16–42. [CrossRef]
89. Al-Kattan, A.; Wichser, A.; Vonbank, R.; Brunner, S.; Ulrich, A.; Zuin, S.; Nowack, B. Release of TiO2 from paints containing pigment-TiO_2 or nano-TiO_2 by weathering. *Environ. Sci. Process. Impacts* **2013**, *15*, 2186–2193. [CrossRef]
90. Jacobs, J.; Poel, I.; Osseweijer, P. Sunscreens with titanium dioxide (TiO_2) nano-particles: A societal experiment. *Nanoethics* **2010**, *4*, 103–113. [CrossRef]
91. Rompelberg, C.; Heringa, M.B.; van Donkersgoed, G.; Drijvers, J.; Roos, A.; Westenbrink, S.; Peters, R.; van Bemmel, G.; Brand, W.; Oomen, A.G. Oral intake of added titanium dioxide and its nanofraction from food products, food supplements and toothpaste by the Dutch population. *Nanotoxicology* **2016**, *10*, 1404–1414. [CrossRef] [PubMed]
92. Hanaor, D.A.H.; Sorrell, C.C. Review of the anatase to rutile phase transformation. *J. Mater. Sci.* **2011**, *46*, 855–874. [CrossRef]
93. Chen, X.; Mao, S.S. Titanium dioxide nanomaterials: Synthesis, properties, modifications, and applications. *Chem. Rev.* **2007**, *107*, 2891–2959. [CrossRef] [PubMed]
94. Abbasi, S. Photocatalytic activity study of coated anatase-rutile titania nanoparticles with nanocrystalline tin dioxide based on the statistical analysis. *Environ. Monit. Assess.* **2019**, *191*, 206–218. [CrossRef] [PubMed]
95. Pei, D.-N.; Gong, L.; Zhang, A.-Y.; Zhang, X.; Chen, J.-J.; Mu, Y.; Yu, H.-Q. Defective titanium dioxide single crystals exposed by high-energy {001} facets for efficient oxygen reduction. *Nat. Commun.* **2015**, *6*, 8696. [CrossRef] [PubMed]
96. Ye, F.X.; Ohmori, A.; Tsumura, T.; Nakata, K.; Li, C.J. Microstructural analysis and photocatalytic activity of plasma-sprayed titania-hydroxyapatite coatings. *J. Therm. Spray Technol.* **2007**, *16*, 776–782. [CrossRef]
97. Ren, K.; Liu, Y.; He, X.; Li, H. Suspension plasma spray fabrication of nanocrystalline titania hollow microspheres for photocatalytic applications. *J. Therm. Spray Technol.* **2015**, *24*, 1213–1220. [CrossRef]
98. Luttrell, T.; Halpegamage, S.; Tao, J.; Kramer, A.; Sutter, E.; Batzill, M. Why is anatase a better photocatalyst than rutile?—Model studies on epitaxial TiO_2 films. *Sci. Rep.* **2014**, *4*, 4043. [CrossRef]
99. Fresno, F.; Portela, R.; Suárez, S.; Coronado, J.M. Photocatalytic materials: Recent achievements and near future trends. *J. Mater. Chem. A* **2014**, *2*, 2863–2884. [CrossRef]
100. Setvin, M.; Aschauer, U.; Hulva, J.; Simschitz, T.; Daniel, B.; Schmid, M.; Selloni, A.; Diebold, U. Following the reduction of oxygen on TiO_2 anatase (101) step by step. *J. Am. Chem. Soc.* **2016**, *138*, 9565–9571. [CrossRef]
101. Hoffmann, M.R.; Martin, S.T.; Choi, W.; Bahnemann, D.W. Environmental applications of semiconductor photocatalysis. *Chem. Rev.* **1995**, *95*, 69–96. [CrossRef]
102. Ali, I.; Suhail, M.; Alothman, Z.A.; Alwarthan, A. Recent advances in syntheses, properties and applications of TiO_2 nanostructures. *RSC Adv.* **2018**, *8*, 30125–30147. [CrossRef] [PubMed]
103. Nowotny, M.K.; Bak, T.; Nowotny, J. Electrical properties and defect chemistry of TiO_2 single crystal. I. Electrical conductivity. *J. Phys. Chem. B* **2006**, *110*, 16270–16282. [CrossRef] [PubMed]
104. Fujitsu, S.; Hamada, T. Electrical properties of manganese-doped titanium dioxide. *J. Am. Ceram. Soc.* **1994**, *77*, 3281–3283. [CrossRef]

105. Lu, L.; Xia, X.; Luo, J.K.; Shao, G. Mn-doped TiO_2 thin films with significantly improved optical and electrical properties. *J. Phys. D Appl. Phys.* **2012**, *45*, 485102. [CrossRef]
106. Wang, Y.; Cheng, H.; Hao, Y.; Ma, J.; Li, W.; Cai, S. Preparation, characterization and photoelectrochemical behaviors of Fe(III)-doped TiO_2 nanoparticles. *J. Mater. Sci.* **1999**, *34*, 3721–3729. [CrossRef]
107. Bally, A.R.; Korobeinikova, E.; Schmid, P.; Lévy, F.; Bussy, F. Structural and electrical properties of Fe-doped TiO_2 thin films. *J. Phys. D Appl. Phys.* **1999**, *31*, 1149. [CrossRef]
108. Li, Z.; Ding, D.; Liu, Q.; Ning, C.; Wang, X. Ni-doped TiO_2 nanotubes for wide-range hydrogen sensing. *Nanoscale Res. Lett.* **2014**, *9*, 118. [CrossRef]
109. Li, Y.; Wlodarski, W.; Galatsis, K.; Moslih, S.; Cole, J.; Russo, S.; Rockelmann, N. Gas sensing properties of P-type semiconducting Cr-doped TiO_2 thin films. *Sens. Actuators B Chem.* **2002**, *83*, 160–163. [CrossRef]
110. Ruiz, A.; Cornet, A.; Sakai, G.; Shimanoe, K.; Morante, J.; Yamazoe, N. Preparation of Cr-doped TiO_2 thin film of p-type conduction for gas sensor application. *Chem. Lett.* **2002**, *31*, 892–893. [CrossRef]
111. Cao, J.; Zhang, Y.; Liu, L.; Ye, J. A p-type Cr-doped TiO_2 photo-electrode for photo-reduction. *Chem. Commun.* **2013**, *49*, 3440–3442. [CrossRef] [PubMed]
112. Shao, B.; Feng, M.; Zuo, X. Carrier-dependent magnetic anisotropy of cobalt doped titanium dioxide. *Sci. Rep.* **2014**, *4*, 7496. [CrossRef] [PubMed]
113. Lontio Fomekong, R.; Saruhan, B. Synthesis of Co^{3+} doped TiO_2 by co-precipitation route and its gas sensing properties. *Front. Mater.* **2019**, *6*, 1–6. [CrossRef]
114. Sathasivam, S.; Bhachu, D.S.; Lu, Y.; Chadwick, N.; Althabaiti, S.A.; Alyoubi, A.O.; Basahel, S.N.; Carmalt, C.J.; Parkin, I.P. Tungsten doped TiO_2 with enhanced photocatalytic and optoelectrical properties via aerosol assisted chemical vapor deposition. *Sci. Rep.* **2015**, *5*, 10952. [CrossRef]
115. He, S.; Meng, Y.; Cao, Y.; Huang, S.; Yang, J.; Tong, S.; Wu, M. Hierarchical Ta-doped TiO_2 nanorod arrays with improved charge separation for photoelectrochemical water oxidation under FTO side illumination. *Nanomaterials* **2018**, *8*, 983. [CrossRef] [PubMed]
116. Biedrzycki, J.; Livraghi, S.; Giamello, E.; Agnoli, S.; Granozzi, G. Fluorine- and niobium-doped TiO_2: Chemical and spectroscopic properties of polycrystalline n-type-doped anatase. *J. Phys. Chem. C* **2014**, *118*, 8462–8473. [CrossRef]
117. Eguchi, R.; Takekuma, Y.; Ochiai, T.; Nagata, M. Improving interfacial charge-transfer transitions in Nb-doped TiO_2 electrodes with 7,7,8,8-Tetracyanoquinodimethane. *Catalysts* **2018**, *8*, 367. [CrossRef]
118. Ansari, S.; Khan, M.M.; Ansari, M.; Cho, M.H. Nitrogen-doped titanium dioxide (N-doped TiO_2) for visible light photocatalysis. *New J. Chem.* **2016**, *40*, 3000–3009. [CrossRef]
119. Asahi, R.; Morikawa, T.; Irie, H.; Ohwaki, T. Nitrogen-doped titanium dioxide as visible-light-sensitive photocatalyst: Designs, developments, and prospects. *Chem. Rev.* **2014**, *114*, 9824–9852. [CrossRef]
120. Kim, T.H.; Go, G.-M.; Cho, H.-B.; Song, Y.; Lee, C.-G.; Choa, Y.-H. A novel synthetic method for N doped TiO_2 nanoparticles through plasma-assisted electrolysis and photocatalytic activity in the visible region. *Front. Chem.* **2018**, *6*, 458. [CrossRef]
121. Yang, G.; Jiang, Z.; Shi, H.; Xiao, T.; Yan, Z. Preparation of highly visible-light active N-doped TiO_2 photocatalyst. *J. Mater. Chem.* **2010**, *20*, 5301–5309. [CrossRef]
122. Zhang, X.; Zhou, J.; Gu, Y.; Fan, D. Visible-light photocatalytic activity of N-doped TiO_2 nanotube arrays on acephate degradation. *J. Nanomater.* **2015**, *2015*, 527070. [CrossRef]
123. Agyeman, D.A.; Song, K.; Kang, S.H.; Jo, M.R.; Cho, E.; Kang, Y.-M. An improved catalytic effect of nitrogen-doped TiO_2 nanofibers for rechargeable Li–O_2 batteries; the role of oxidation states and vacancies on the surface. *J. Mater. Chem. A* **2015**, *3*, 22557–22563. [CrossRef]
124. Asahi, R.; Morikawa, T. Nitrogen complex species and its chemical nature in TiO_2 for visible-light sensitized photocatalysis. *Chem. Phys.* **2007**, *339*, 57–63. [CrossRef]
125. Peng, F.; Cai, L.; Yu, H.; Wang, H.; Yang, J. Synthesis and characterization of substitutional and interstitial nitrogen-doped titanium dioxides with visible light photocatalytic activity. *J. Solid State Chem.* **2008**, *181*, 130–136. [CrossRef]
126. Zeng, L.; Song, W.; Li, M.; Jie, X.; Zeng, D.; Xie, C. Comparative study on the visible light driven photocatalytic activity between substitutional nitrogen doped and interstitial nitrogen doped TiO_2. *Appl. Catal. A Gen.* **2014**, *488*, 239–247. [CrossRef]
127. Lee, J.; Lee, S.J.; Han, W.B.; Jeon, H.; Park, J.; Kim, H.; Yoon, C.S.; Jeon, H. Effect of crystal structure and grain size on photocatalytic activities of remote-plasma atomic layer deposited titanium oxide thin film. *ECS J. Solid State Sci. Technol.* **2012**, *1*, Q63–Q69. [CrossRef]
128. Retamoso, C.; Escalona, N.; González, M.; Barrientos, L.; Allende-González, P.; Stancovich, S.; Serpell, R.; Fierro, J.L.G.; Lopez, M. Effect of particle size on the photocatalytic activity of modified rutile sand (TiO_2) for the discoloration of methylene blue in water. *J. Photochem. Photobiol. A Chem.* **2019**, *378*, 136–141. [CrossRef]
129. Kočí, K.; Obalová, L.; Matějová, L.; Plachá, D.; Lacný, Z.; Jirkovský, J.; Šolcová, O. Effect of TiO_2 particle size on the photocatalytic reduction of CO_2. *Appl. Catal. B Environ.* **2009**, *89*, 494–502. [CrossRef]
130. Amano, F.; Nogami, K.; Tanaka, M.; Ohtani, B. Correlation between surface area and photocatalytic activity for acetaldehyde decomposition over bismuth tungstate particles with a hierarchical structure. *Langmuir* **2010**, *26*, 7174–7180. [CrossRef]
131. Vorontsov, A.V.; Kabachkov, E.N.; Balikhin, I.L.; Kurkin, E.N.; Troitskii, V.N.; Smirniotis, P.G. Correlation of surface area with photocatalytic activity of TiO_2. *J. Adv. Oxid. Technol.* **2018**, *21*, 127–137. [CrossRef]

132. Cheng, H.; Wang, J.; Zhao, Y.; Han, X. Effect of phase composition, morphology, and specific surface area on the photocatalytic activity of TiO_2 nanomaterials. *RSC Adv.* **2014**, *4*, 47031–47038. [CrossRef]
133. Elgh, B.; Yuan, N.; Cho, H.S.; Magerl, D.; Philipp, M.; Roth, S.V.; Yoon, K.B.; Müller-Buschbaum, P.; Terasaki, O.; Palmqvist, A.E.C. Controlling morphology, mesoporosity, crystallinity, and photocatalytic activity of ordered mesoporous TiO_2 films prepared at low temperature. *APL Mater.* **2014**, *2*, 113313. [CrossRef]
134. Tanaka, K.; Capule, M.F.V.; Hisanaga, T. Effect of crystallinity of TiO_2 on its photocatalytic action. *Chem. Phys. Lett.* **1991**, *187*, 73–76. [CrossRef]
135. Chen, W.-T.; Chan, A.; Jovic, V.; Sun-Waterhouse, D.; Murai, K.-i.; Idriss, H.; Waterhouse, G.I.N. Effect of the TiO_2 crystallite size, TiO_2 polymorph and test conditions on the photo-oxidation rate of aqueous methylene blue. *Top. Catal.* **2015**, *58*, 85–102. [CrossRef]
136. Yuan, B.; Wang, Y.; Bian, H.; Shen, T.; Wu, Y.; Chen, Z. Nitrogen doped TiO_2 nanotube arrays with high photoelectrochemical activity for photocatalytic applications. *Appl. Surf. Sci.* **2013**, *280*, 523–529. [CrossRef]
137. Peng, F.; Cai, L.; Huang, L.; Yu, H.; Wang, H. Preparation of nitrogen-doped titanium dioxide with visible-light photocatalytic activity using a facile hydrothermal method. *J. Phys. Chem. Solids* **2008**, *69*, 1657–1664. [CrossRef]
138. Di Valentin, C.; Pacchioni, G.; Selloni, A.; Livraghi, S.; Giamello, E. Characterization of paramagnetic species in N-Doped TiO_2 powders by EPR spectroscopy and DFT calculations. *J. Phys. Chem. B* **2005**, *109*, 11414–11419. [CrossRef]
139. Dong, F.; Zhao, W.; Wu, Z.; Guo, S. Band structure and visible light photocatalytic activity of multi-type nitrogen doped TiO_2 nanoparticles prepared by thermal decomposition. *J. Hazard. Mater.* **2009**, *162*, 763–770. [CrossRef]
140. Di Valentin, C.; Finazzi, E.; Pacchioni, G.; Selloni, A.; Livraghi, S.; Paganini, M.C.; Giamello, E. N-doped TiO_2: Theory and experiment. *Chem. Phys.* **2007**, *339*, 44–56. [CrossRef]
141. Weibel, A.; Bouchet, R.; Knauth, P. Electrical properties and defect chemistry of anatase (TiO_2). *Solid State Ion.* **2006**, *177*, 229–236. [CrossRef]
142. Byl, O.; Yates, J.T. Anisotropy in the electrical conductivity of rutile TiO_2 in the (110) plane. *J. Phys. Chem. B* **2006**, *110*, 22966–22967. [CrossRef] [PubMed]
143. Demetry, C.; Shi, X. Grain size-dependent electrical properties of rutile (TiO_2). *Solid State Ion.* **1999**, *118*, 271–279. [CrossRef]
144. Johnson, G.; Weyl, W.A. Influence of minor additions on color and electrical properties of rutile*. *J. Am. Ceram. Soc.* **1949**, *32*, 398–401. [CrossRef]
145. Dang, Y.; West, A.R. Oxygen stoichiometry, chemical expansion or contraction, and electrical properties of rutile, $TiO_{2\pm\delta}$ ceramics. *J. Am. Ceram. Soc.* **2019**, *102*, 251–259. [CrossRef]
146. Hong, M.; Dai, L.; Li, H.; Hu, H.; Liu, K.; Linfei, Y.; Pu, C. Structural phase transition and metallization of nanocrystalline rutile investigated by high-pressure raman spectroscopy and electrical conductivity. *Minerals* **2019**, *9*, 441. [CrossRef]
147. Bak, T.; Nowotny, J.; Stranger, J. Electrical properties of TiO_2: Equilibrium vs dynamic electrical conductivity. *Ionics* **2010**, *16*, 673–679. [CrossRef]
148. Nowotny, J. *Oxide Semiconductors for Solar Energy Conversion*; CRC Press: Boca Raton, FL, USA, 2016.
149. Grundmann, M. *The Physics of Semiconductors: An Introduction Including Nanophysics and Applications*; Springer: Berlin/Heidelberg, Germany, 2010.
150. Ding, Z.; Lu, G.Q.; Greenfield, P.F. Role of the crystallite phase of TiO_2 in heterogeneous photocatalysis for phenol oxidation in water. *J. Phys. Chem. B* **2000**, *104*, 4815–4820. [CrossRef]
151. Li, Z.; Cong, S.; Xu, Y. Brookite vs anatase TiO_2 in the photocatalytic activity for organic degradation in water. *ACS Catal.* **2014**, *4*, 3273–3280. [CrossRef]
152. Tran, H.T.T.; Kosslick, H.; Ibad, M.F.; Fischer, C.; Bentrup, U.; Vuong, T.H.; Nguyen, L.Q.; Schulz, A. Photocatalytic performance of highly active brookite in the degradation of hazardous organic compounds compared to anatase and rutile. *Appl. Catal. B Environ.* **2017**, *200*, 647–658. [CrossRef]
153. Kaplan, R.; Erjavec, B.; Pintar, A. Enhanced photocatalytic activity of single-phase, nanocomposite and physically mixed TiO_2 polymorphs. *Appl. Catal. A Gen.* **2015**, *489*, 51–60. [CrossRef]
154. Vequizo, J.J.M.; Matsunaga, H.; Ishiku, T.; Kamimura, S.; Ohno, T.; Yamakata, A. Trapping-induced enhancement of photocatalytic activity on brookite TiO_2 powders: Comparison with anatase and rutile TiO_2 powders. *ACS Catal.* **2017**, *7*, 2644–2651. [CrossRef]
155. Tran, T.T.H.; Kosslick, H.; Schulz, A.; Nguyen, Q.L. Photocatalytic performance of crystalline titania polymorphs in the degradation of hazardous pharmaceuticals and dyes. *Adv. Nat. Sci. Nanosci. Nanotechnol.* **2017**, *8*, 015011. [CrossRef]
156. Kandiel, T.A.; Robben, L.; Alkaim, A.; Bahnemann, D. Brookite versus anatase TiO_2 photocatalysts: Phase transformations and photocatalytic activities. *Photochem. Photobiol. Sci.* **2013**, *12*, 602–609. [CrossRef]
157. Fischer, K.; Gawel, A.; Rosen, D.; Krause, M.; Latif, A.; Griebel, J.; Prager, A.; Schulze, A. Low-temperature synthesis of anatase/rutile/brookite TiO_2 nanoparticles on a polymer membrane for photocatalysis. *Catalysts* **2017**, *7*, 209. [CrossRef]
158. Farhadian Azizi, K.; Bagheri-Mohagheghi, M.M. Transition from anatase to rutile phase in titanium dioxide (TiO_2) nanoparticles synthesized by complexing sol–gel process: Effect of kind of complexing agent and calcinating temperature. *J. Sol-Gel Sci. Technol.* **2013**, *65*, 329–335. [CrossRef]
159. Zhou, Y.; Fichthorn, K.A. Microscopic view of nucleation in the anatase-to-rutile transformation. *J. Phys. Chem. C* **2012**, *116*, 8314–8321. [CrossRef]

160. Byrne, C.; Fagan, R.; Hinder, S.; McCormack, D.E.; Pillai, S.C. New approach of modifying the anatase to rutile transition temperature in TiO_2 photocatalysts. *RSC Adv.* **2016**, *6*, 95232–95238. [CrossRef]
161. Wu, Q.; Li, D.; Hou, Y.; Wu, L.; Fu, X.; Wang, X. Study of relationship between surface transient photoconductivity and liquid-phase photocatalytic activity of titanium dioxide. *Mater. Chem. Phys.* **2007**, *102*, 53–59. [CrossRef]
162. Bokare, A.; Pai, M.; Athawale, A.A. Surface modified Nd doped TiO_2 nanoparticles as photocatalysts in UV and solar light irradiation. *Sol. Energy* **2013**, *91*, 111–119. [CrossRef]
163. Zhang, W.; Li, X.; Jia, G.; Gao, Y.; Wang, H.; Cao, Z.; Li, C.; Liu, J. Preparation, characterization, and photocatalytic activity of boron and lanthanum co-doped TiO_2. *Catal. Commun.* **2014**, *45*, 144–147. [CrossRef]
164. Alijani, M.; Najibi ilkhechi, N. Effect of Ni doping on the structural and optical properties of TiO_2 nanoparticles at various concentration and temperature. *Silicon* **2018**, *10*, 2569–2575. [CrossRef]
165. Wang, G.Q.; Lan, W.; Han, G.J.; Wang, Y.; Su, Q.; Liu, X.Q. Effect of Nb doping on the phase transition and optical properties of sol–gel TiO_2 thin films. *J. Alloys Compd.* **2011**, *509*, 4150–4153. [CrossRef]
166. Fernández-García, M.; Martínez-Arias, A.; Hanson, J.C.; Rodriguez, J.A. Nanostructured oxides in chemistry: Characterization and properties. *Chem. Rev.* **2004**, *104*, 4063–4104. [CrossRef]
167. Akhtar, M.K.; Pratsinis, S.E.; Mastrangelo, S.V.R. Dopants in vapor-phase synthesis of titania powders. *J. Am. Ceram. Soc.* **1992**, *75*, 3408–3416. [CrossRef]
168. Nyamukamba, P.; Tichagwa, L.; Greyling, C. The influence of carbon doping on TiO_2 nanoparticle size, surface area, anatase to rutile phase transformation and photocatalytic activity. *Mater. Sci. Forum* **2012**, *712*, 49–63. [CrossRef]
169. Bu, X.; Zhang, G.; Zhang, C. Effect of nitrogen doping on anatase–rutile phase transformation of TiO_2. *Appl. Surf. Sci.* **2012**, *258*, 7997–8001. [CrossRef]
170. Yu, J.C.; Yu, J.; Ho, W.; Jiang, Z.; Zhang, L. Effects of F- doping on the photocatalytic activity and microstructures of nanocrystalline TiO_2 powders. *Chem. Mater.* **2002**, *14*, 3808–3816. [CrossRef]
171. Singh, V.; Rao, A.; Tiwari, A.; Yashwanth, P.; Lal, M.; Dubey, U.; Aich, S.; Roy, B. Study on the effects of Cl and F doping in TiO_2 powder synthesized by a sol-gel route for biomedical applications. *J. Phys. Chem. Solids* **2019**, *134*, 262–272. [CrossRef]
172. Shannon, R.D.; Pask, J.A. Kinetics of the anatase-rutile transformation. *J. Am. Ceram. Soc.* **1965**, *48*, 391–398. [CrossRef]
173. Qian, R.; Zong, H.; Schneider, J.; Zhou, G.; Zhao, T.; Li, Y.; Yang, J.; Bahnemann, D.W.; Pan, J.H. Charge carrier trapping, recombination and transfer during TiO_2 photocatalysis: An overview. *Catal. Today* **2019**, *335*, 78–90. [CrossRef]
174. Zhang, J.; Zhou, P.; Liu, J.; Yu, J. New understanding of the difference of photocatalytic activity among anatase, rutile and brookite TiO_2. *Phys. Chem. Chem. Phys.* **2014**, *16*, 20382–20386. [CrossRef] [PubMed]
175. Madhusudan Reddy, K.; Manorama, S.V.; Ramachandra Reddy, A. Bandgap studies on anatase titanium dioxide nanoparticles. *Mater. Chem. Phys.* **2003**, *78*, 239–245. [CrossRef]
176. Soares, G.B.; Ribeiro, R.A.P.; de Lazaro, S.R.; Ribeiro, C. Photoelectrochemical and theoretical investigation of the photocatalytic activity of TiO_2:N. *RSC Adv.* **2016**, *6*, 89687–89698. [CrossRef]
177. Odling, G.; Robertson, N. Why is anatase a better photocatalyst than rutile? The importance of free hydroxyl radicals. *ChemSusChem* **2015**, *8*, 1838–1840. [CrossRef]
178. Chatzitakis, A.; Sartori, S. Recent advances in the use of black TiO_2 for production of hydrogen and other solar fuels. *ChemPhysChem* **2019**, *20*, 1272–1281. [CrossRef]
179. Zhou, X.; Liu, N.; Schmuki, P. Photocatalysis with TiO_2 nanotubes: "Colorful" reactivity and designing site-specific photocatalytic centers into TiO_2 nanotubes. *ACS Catal.* **2017**, *7*, 3210–3235. [CrossRef]
180. Ullattil, S.G.; Narendranath, S.B.; Pillai, S.C.; Periyat, P. Black TiO_2 nanomaterials: A review of recent advances. *Chem. Eng. J.* **2018**, *343*, 708–736. [CrossRef]
181. Liu, Y.; Tian, L.; Tan, X.; Li, X.; Chen, X. Synthesis, properties, and applications of black titanium dioxide nanomaterials. *Sci. Bull.* **2017**, *62*, 431–441. [CrossRef]
182. Chen, X.; Liu, L.; Yu, P.Y.; Mao, S.S. Increasing solar absorption for photocatalysis with black hydrogenated titanium dioxide nanocrystals. *Science* **2011**, *331*, 746. [CrossRef]
183. Naldoni, A.; Altomare, M.; Zoppellaro, G.; Liu, N.; Kment, Š.; Zbořil, R.; Schmuki, P. Photocatalysis with reduced TiO_2: From black TiO_2 to cocatalyst-free hydrogen production. *ACS Catal.* **2019**, *9*, 345–364. [CrossRef] [PubMed]
184. Coto, M.; Divitini, G.; Dey, A.; Krishnamurthy, S.; Ullah, N.; Ducati, C.; Kumar, R.V. Tuning the properties of a black TiO_2-Ag visible light photocatalyst produced by a rapid one-pot chemical reduction. *Mater. Today Chem.* **2017**, *4*, 142–149. [CrossRef]
185. Song, H.; Li, C.; Lou, Z.; Ye, Z.; Zhu, L. Effective formation of oxygen vacancies in black TiO_2 nanostructures with efficient solar-driven water splitting. *ACS Sustain. Chem. Eng.* **2017**, *5*, 8982–8987. [CrossRef]
186. Chen, S.; Xiao, Y.; Wang, Y.; Hu, Z.; Zhao, H.; Xie, W. A Facile Approach to prepare black TiO_2 with oxygen vacancy for enhancing photocatalytic activity. *Nanomaterials* **2018**, *8*, 245. [CrossRef] [PubMed]
187. Cui, H.; Zhao, W.; Yang, C.; Yin, H.; Lin, T.; Shan, Y.; Xie, Y.; Gu, H.; Huang, F. Black TiO_2 nanotube arrays for high-efficiency photoelectrochemical water-splitting. *J. Mater. Chem. A* **2014**, *2*, 8612–8616. [CrossRef]
188. Lepcha, A.; Maccato, C.; Mettenbörger, A.; Andreu, T.; Mayrhofer, L.; Walter, M.; Olthof, S.; Ruoko, T.P.; Klein, A.; Moseler, M.; et al. Electrospun black titania nanofibers: Influence of hydrogen plasma-induced disorder on the electronic structure and photoelectrochemical performance. *J. Phys. Chem. C* **2015**, *119*, 18835–18842. [CrossRef]

189. Singh, A.P.; Kodan, N.; Mehta, B.R.; Dey, A.; Krishnamurthy, S. In-situ plasma hydrogenated TiO_2 thin films for enhanced photoelectrochemical properties. *Mater. Res. Bull.* **2016**, *76*, 284–291. [CrossRef]
190. Xu, C.; Song, Y.; Lu, L.; Cheng, C.; Liu, D.; Fang, X.; Chen, X.; Zhu, X.; Li, D. Electrochemically hydrogenated TiO_2 nanotubes with improved photoelectrochemical water splitting performance. *Nanoscale Res. Lett.* **2013**, *8*, 391. [CrossRef]
191. Wang, J.; Yang, P.; Huang, B. Self-doped TiO_2-x nanowires with enhanced photocatalytic activity: Facile synthesis and effects of the Ti^{3+}. *Appl. Surf. Sci.* **2015**, *356*, 391–398. [CrossRef]
192. Teng, F.; Li, M.; Gao, C.; Zhang, G.; Zhang, P.; Wang, Y.; Chen, L.; Xie, E. Preparation of black TiO_2 by hydrogen plasma assisted chemical vapor deposition and its photocatalytic activity. *Appl. Catal. B Environ.* **2014**, *148–149*, 339–343. [CrossRef]
193. Tian, J.; Leng, Y.; Cui, H.; Liu, H. Hydrogenated TiO_2 nanobelts as highly efficient photocatalytic organic dye degradation and hydrogen evolution photocatalyst. *J. Hazard. Mater.* **2015**, *299*, 165–173. [CrossRef] [PubMed]
194. Sarkar, A.; Khan, G.G. The formation and detection techniques of oxygen vacancies in titanium oxide-based nanostructures. *Nanoscale* **2019**, *11*, 3414–3444. [CrossRef] [PubMed]
195. Pan, X.; Yang, M.-Q.; Fu, X.; Zhang, N.; Xu, Y.-J. Defective TiO_2 with oxygen vacancies: Synthesis, properties and photocatalytic applications. *Nanoscale* **2013**, *5*, 3601–3614. [CrossRef]
196. Zhao, H.; Pan, F.; Li, Y. A review on the effects of TiO_2 surface point defects on CO_2 photoreduction with H_2O. *J. Materiomics* **2017**, *3*, 17–32. [CrossRef]
197. Liu, G.; Yin, L.-C.; Wang, J.; Niu, P.; Zhen, C.; Xie, Y.; Cheng, H.-M. A red anatase TiO_2 photocatalyst for solar energy conversion. *Energy Environ. Sci.* **2012**, *5*, 9603–9610. [CrossRef]
198. Yang, Y.; Yin, L.-C.; Gong, Y.; Niu, P.; Wang, J.-Q.; Gu, L.; Chen, X.; Liu, G.; Wang, L.; Cheng, H.-M. An unusual strong visible-light absorption band in red anatase TiO_2 photocatalyst induced by atomic hydrogen-occupied oxygen vacancies. *Adv. Mater.* **2018**, *30*, 1704479. [CrossRef] [PubMed]